Inertia Effects in Falling Liquid Films. Part I: Modelling and Regularization Part II: Secondary Instability and 3D waves

Benoit Scheid
Microgravity Research Center
Université Libre de Bruxelles, Belgium

Abstract

Previous attempts at the modeling of film flows down an inclined plane are reviewed, focusing on the limit of each formulation. A Padé approximant technique has been applied to derive a *regularized model* formulated in terms of two coupled evolution equations for the film thickness h and the flow rate q. This model accounts for inertia effects due to the deviations of the velocity profile from the parabolic shape, and closely sticks to the asymptotic long-wave expansion in the appropriate limit. The *regularized model* is next extended to include spanwise dependence. The stability of two-dimensional traveling waves against three-dimensional perturbations is investigated. The secondary instability is found to be not really selective which explains the widespread presence of the synchronous instability observed in the experiments by Liu *et al.* (1995), though theory predicts in most cases a subharmonic scenario. Three-dimensional wave patterns are next computed assuming periodic boundary conditions. Transition from 2D to 3D flows is shown to be strongly dependent on initial conditions. The herringbone patterns, the synchronously deformed fronts and the three-dimensional solitary waves observed in experiments (Liu *et al.*, 1995; Park & Nosoko, 2003; Alekseenko *et al.*, 1994) are recovered using our three-equation regularized model, which is found to be an excellent compromise between the *complete model*, which has seven equations, and the *simplified model*, which does not include the second-order inertia corrections. Those corrections were found to be decisive in capturing the nature of the secondary instability as well as the spanwise wavelength of the emerging pattern.

Contents

1 Introduction

Thin films flowing down inclines have a rich dynamics extensively studied for a long time since Kapitza's experimental and theoretical pioneering work at the end of the forties (Kapitza, 1948; Kapitza & Kapitza, 1949). Besides their importance for engineering applications (*e.g.* evaporators or chemical reactors), their interest mainly stems from the fact that their evolution is amenable to thorough theoretical analysis. This situation happens mostly due to the two-dimensional, long-wavelengthed, supercritical character of the primary instability mode. Thickness modulations which develop over initially uniform films are usually spanwise homogeneous and slowly varying both in time and in space. Technically, the slow space dependence allows gradient expansions in terms of a small parameter ϵ, called the *film parameter*, basically measuring the slope of the interface in order of magnitude. A lubrication approximation relying on this expansion further allows the

elimination of most of the cross-stream dependence of the flow. The approach is thus similar to that followed in the study of boundary layers and deep analogies can be found in the transition to turbulence of each system, especially at the level of secondary instabilities.
These notes are divided in two parts. Part I focuses on the film's dynamics when spanwise modulations are forbidden, a case called two-dimensional in the following. This assumption is relaxed in Part II devoted to the full three-dimensional case, secondary instabilities and comparisons with experimental results.* The rest of this introduction is devoted to a brief review of the phenomenology and theoretical settings, motivated by the lack of a clear presentation of the limits and hypotheses sustaining the different approaches in the literature, and the connection of the modeling developed here to the work by Ooshida (1999).

1.1 Phenomenology

Many experimental studies have been devoted to the wavy regime of film flows since the first observations by Kapitza (1948) and Kapitza & Kapitza (1949). Most of them are referred to in the review by Alekseenko *et al.* (1994). More recent experimental results are presented for example in Nosoko *et al.* (1996), Vlachogiannis & Bontozoglou (2001), Park & Nosoko (2003), Nosoko & Miyara (2004), or Argyriadi *et al.* (2004). Gollub and coworkers have performed an extensive study of water-glycerin mixtures flowing down weakly inclined planes, see Liu *et al.* (1993), Liu & Gollub (1993), Liu & Gollub (1994), and Liu *et al.* (1995). Controlling the entrance flow rate, they applied a periodic forcing at the inlet and observed the response of the film at given frequency. Their experiments give the clearest picture of the phenomenology of interacting waves on film flows, coming and completing the review by Chang *et al.* (1994). The observations are schematically summarized in figure 1. Four stages corresponding each to a different region can be identified by following the flow along the inclined plane.
The inception region is the domain close to the inlet where the primary linear instability of the flat film develops in space. Squire's theorem stipulating that the most dangerous perturbations are spanwise-independent has been shown to apply to free surface flows by Yih (1955), which theoretically backs the fact that observed primary waves are two-dimensional (2D).
The amplitude of the wave next saturates and its shape remains unchanged over distances corresponding to a few wavelengths (Region II). These waves are slow and present wide bumpy crests and deep thin troughs. They belong to the γ_1 family in the terminology introduced by Chang *et al.* (1993). The rest of the story depends on the forcing frequency.
At low frequency (figure 1, top) saturated waves experience a secondary instability which, close to the threshold, remains 2D ending in large amplitude solitary waves in the form of fast humps preceded by small capillary

*Two vs. three dimensional refer to the fluid velocity dependence. Two dimensional flow means spanwise independent (coordinates x and y) while the surface elevation is one-dimensionally modulated (along x). On the other hand, full three dimensional flow (x, y, z) involves two-dimensional thickness modulations (x, z).

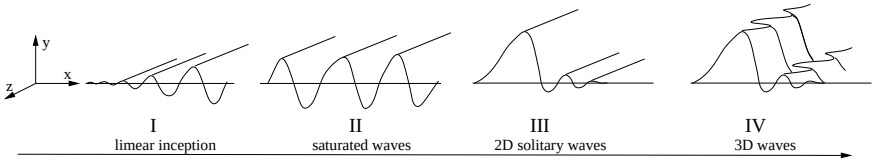

(a) low frequency

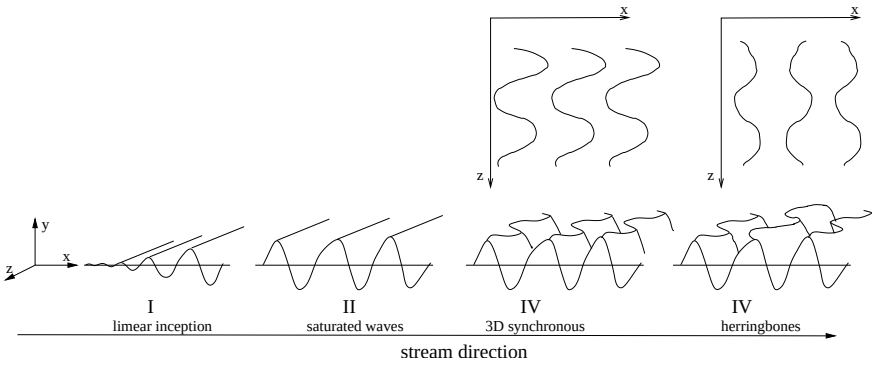

(b) high frequency

Figure 1: Phenomenological sketch of the spatial evolution of film flows, after Chang *et al.* (1994); Liu *et al.* (1995).

ripples (Region III). Such waves belong to the γ_2 family. They are generally unstable against transverse perturbations which leads to the last stage of secondary three-dimensional instabilities (Region IV).

At larger frequencies (figure 1, bottom) Liu *et al.* reported two different scenarios that are strongly reminiscent of what happens in boundary layers (Schmid & Henningson, 2001). The first one, referred to as a *synchronous* mode, is characterized by wave crests deformed in phase in the spanwise direction. The second one, less commonly observed, appears when two successive crests are deformed with a phase shift of π. This leads to checkerboard (or herringbone) patterns characteristic of a streamwise subharmonic instability combined to a spanwise modulation. These two modes are reminiscent of aligned and staggered Λ-vortices developing in transitional boundary layers, thus analogous to the type-K and type-H transitions, respectively (Herbert, 1988). At high enough forcing frequency, the flow becomes disordered before the 2D solitary waves have a chance to appear because 3D instabilities are stronger than the 2D mode, which explains the absence of Region III in the corresponding picture.

Finally, at very low forcing frequencies, saturated γ_1 waves (Region II) do not show up while solitary wave of the γ_2 family directly obtains, which testifies for a continuity of the film's behavior as the frequency is varied.

1.2 Theoretical issues

The separation of scales enabled by the long wavelength instability allows one to reduce the dimensionality of the basic equations. Prandtl's simplification of the cross-stream momentum equation —usual in boundary layer theory— can be applied here and helps one to get rid of the in-depth pressure distribution dominated here by surface tension and gravity. This leads to so-called boundary-layer equations, see Chang *et al.* (1993) for a detailed presentation. These equations can be viewed as the first step of the long-wave expansion performed by Benney (1966). Modulations of the film thickness around the flat film solution being slow in space and time, the product ϵR is small as in classical lubrication theory. Inertia is thus small and consequently the velocity field stays enslaved to the evolution of the film thickness. This leads to a single evolution equation for the film thickness governing the dynamics of the flow at the onset of the instability. An alternative to the gradient expansion approach is to make use of the Kármán–Polhausen averaging technique as in the boundary-layer theory (Schlichting, 1979). This technique, which was first proposed by Kapitza (1948) and later reinvestigated by Shkadov (1967), leads to a two-field model involving the film thickness h and the local flow rate q, for which the velocity field is not supposed to be entirely slaved to the film thickness evolution.
The transition of film flows towards 3D dynamics was first theoretically investigated in this context by Trifonov (1989). Starting from 2D solutions to the Kapitza–Shkadov model computed at rest in a moving frame, he analyzed their stability against transverse modulations and showed that the subharmonic instability was always the most dangerous one. The stationary 3D waves bifurcating from the 2D waves of the γ_1 family were shown to have their troughs growing faster than the peaks transverse modulations, which eventually produced trains of isolated depressions, as experimentally observed by Liu *et al.* (1995). Chang (1994) attempted to complete Trifonov's study by using the boundary layer equations. Their stability analysis of the γ_1 family predicted only the subharmonic instability, hence a scenario different from the one reported by Liu and Gollub. Trifonov and Chang *et al.* both only considered vertical walls whereas the experiments at Haverford were performed for an inclined wall where hydrostatic pressure plays a significant role. To our knowledge, there is as yet no thorough theoretical understanding of the full experimental results and especially of the 3D synchronous instability of the slow saturated γ_1 waves.

Part I
Modelling and Regularization Technique

2 Governing equations

2.1 Primitive equations

The flow of a Newtonian liquid down a plane making an angle β with the horizontal is considered. Coordinate x defines the streamwise direction, y denotes the direction normal to the plane, and z is along the spanwise direction. $\mathbf{u} = (u, v, w)$ is the velocity field and p is the pressure. Surface tension σ, viscosity μ, density ρ, are supposed to remain constant. The dimensionless form of the governing equations is obtained with length and time scales based on the kinematic viscosity $\nu = \mu/\rho$ and the streamwise gravity acceleration $g \sin\beta$ so that they depend only on the physical properties of the fluid and the inclination angle. They read:

$$l_\nu = \nu^{2/3}(g\sin\beta)^{-1/3} \qquad \text{and} \qquad t_\nu = \nu^{1/3}(g\sin\beta)^{-2/3}.$$

This scaling is appropriate provided that $\sin\beta \sim O(1)$, i.e. excluding near-horizontal configurations, for which instabilities typical of wall flows set in, involving Tollmien–Schlichting waves of shear-viscous origin, see e.g. Floryan *et al.* (1987). The flow conditions can further be characterized by the dimensionless thickness of the flat film solution (Nusselt flow), h_N, the inclination $B = \cot\beta$ and the Kapitza number $\Gamma = \sigma/\left[\rho\nu^{4/3}(g\sin\beta)^{1/3}\right]$ which compares the surface stress σ/l_ν to the viscous stress μ/t_ν. Using these scales, the Navier-Stokes equation reads:

$$\partial_t\mathbf{u} + \mathbf{u}\cdot\boldsymbol{\nabla}\mathbf{u} = -\boldsymbol{\nabla}p + \boldsymbol{\nabla}^2\mathbf{u} + \mathbf{F}\,. \tag{1}$$

Above and in the following, ∂_α denotes partial differentiation with respect to variable α. $\mathbf{F} = (1, -B, 0)$ represents the dimensionless body force. The continuity equation for an incompressible flow reads:

$$\boldsymbol{\nabla}\cdot\mathbf{u} = 0\,. \tag{2}$$

The evolution equations have to be supplemented with boundary conditions at $y = \tilde{y}$, in practice at the bottom plane, $\tilde{y} = 0$, and at the free surface, $\tilde{y} = h$. A quantity β evaluated at $y = \tilde{y}$ will be denoted by $\beta|_{\tilde{y}}$. The flow is thus subjected to the usual no-slip condition:

$$\mathbf{u}|_0 = 0\,. \tag{3}$$

The interface is governed by the kinematic condition expressing that the free surface is a material surface, that is

$$(\partial_t + \mathbf{u}\cdot\boldsymbol{\nabla})(h(x,z,t) - y) = 0\,,$$

or else

$$v|_h = (\partial_t + u|_h \partial_x + w|_h \partial_z) h \,. \tag{4}$$

Finally, the stress balance at the interface reads:

$$-p\mathbf{n} + (\boldsymbol{\nabla}\mathbf{u} + \boldsymbol{\nabla}\mathbf{u}^T) \cdot \mathbf{n} = -\Gamma(\boldsymbol{\nabla} \cdot \mathbf{n})\mathbf{n} \tag{5}$$

where $\mathbf{n}$ is the unit vector normal to the free surface oriented outwards. Alternatively, Reynolds and Weber numbers based on the entrance flow rate are often preferred though they do not clearly separate flow conditions from the fluid's physical constants. The relations between these dimensionless parameters are easily obtained by noticing that, at the entrance, the interface is flat so that the Reynolds number is related to the Nusselt thickness through an integration of the parabolic velocity profile $u \equiv y\left(h_\mathrm{N} - \frac{1}{2}y^2\right)$ over the depth. This gives:

$$R \equiv q_\mathrm{N} = \tfrac{1}{3} {h_\mathrm{N}}^3 \,, \tag{6}$$

where q_N is the dimensionless Nusselt flow rate. Similarly, the Weber number is related to the Kapitza number through

$$W = \Gamma {h_\mathrm{N}}^{-2} \,. \tag{7}$$

2.2 Boundary layer equations

Comparisons between existing models and the subsequent discussion about needed improvements can be made simpler if the spanwise dependence of the fields ($\partial_z \equiv 0$) is disregarded. Accordingly, in this section and in the rest of Part I, we focus on 2D flows. 3D flows will be considered in Part II. Considering slow space and time variation, the formal parameter ϵ is introduced along with each derivation in space or time $\partial_{x,t} \propto \epsilon$. The assumed slow space variation implies that the velocity component normal to the plane v is much smaller than the streamwise component u, as derived from the continuity equation here rewritten for a 2D flow:

$$\partial_x u + \partial_y v = 0 \,. \tag{8}$$

Consequently, the inertia terms in the y-component of the momentum equation are of higher order and can be dropped out. The remaining equation is then linear and can be integrated to give the pressure distribution up to order ϵ. After substitution of the latter and some algebra detailed in Ruyer-Quil & Manneville (1998), the streamwise momentum equation reads

$$\partial_t u + u\partial_x u + v\partial_y u = 1 + \partial_{yy} u - B\partial_x h + \Gamma \partial_{xxx} h + 2\partial_{xx} u + \partial_x \left[\partial_x u|_h\right] , \tag{9}$$

The no-slip condition (3), is repeated here as:

$$u|_0 = v|_0 = 0 \,, \tag{10}$$

whereas the 2D kinematic condition and the continuity of the tangential stress at the free surface at second order read:

$$\partial_t h + u|_h \partial_x h = v|_h \,, \tag{11}$$

$$\partial_y u|_h = 4\partial_x h \partial_x u|_h - \partial_x v|_h \,. \tag{12}$$

System (8–12) is valid at order ϵ^2 since in the streamwise momentum balance, neglected inertia terms coming from the differentiation of the pressure are effectively of order ϵ^3. Equation (9) is usually referred to as the second-order boundary-layer equation since the assumptions leading to it are essentially the same as those in the derivation of the Prandtl equation of boundary layer theory, see Schlichting (1979).
It should be noted that the main contribution of the surface tension $\Gamma\partial_{xxx}h$ has been retained in (9) though it is formally of order ϵ^3. This is in line with the application of a *least degeneracy principle* that leads one to make all relevant processes appear at lowest order in the formulation by scaling coefficients appropriately, which means here $\Gamma\epsilon \sim O(1)$. This contribution is indeed essential in preventing the steepening and breaking of waves produced by inertia, as discussed *e.g.* by Smith (1990).
Stabilizing agents are capillarity and gravity normal to the plane (as soon as $\beta < \pi/2$). Let us consider the worst case, when the plane is vertical ($\beta = \pi/2$) so that gravity stabilization drops out and surface tension only remains. An estimate of the film parameter ϵ measuring the slope is obtained by balancing the streamwise pressure gradient caused by surface tension $\Gamma\partial_{xxx}h$ with the streamwise gravity acceleration (equal to one in (9)). Defining

$$\kappa = (\Gamma/h_{\rm N}^2)^{1/3} \equiv W^{1/3} \,, \tag{13}$$

this yields $\epsilon \sim 1/\kappa$. Accordingly, we assume in the following that κ, or equivalently the Weber number, is sufficiently large (ϵ sufficiently small) so that the scale decoupling is valid. We also assume that Γ itself is sufficiently large, in practice $\Gamma\epsilon \sim O(1)$ or smaller, which makes $\Gamma\partial_{xxx}h$ the only relevant term formally of order ϵ^3 in the full set of equations (8–12). Combining these conditions one finds $\Gamma h_{\rm N} \sim O(1)$ or smaller, which is a condition on the flow rate, given the fluid properties and the angle β.

2.3 Shkadov's scaling

In practice, we proceed to the rescaling of space variables introduced by Shkadov (1977). At a given inlet flow rate, the natural scale for y is the Nusselt flat film thickness $h_{\rm N}$, which yields the changes $(y, h) = (h_{\rm N}\tilde{y}, h_{\rm N}\tilde{h})$. Then balancing gravity forces and surface tension introduces the scale ratio κ through (13) as discussed above. Shkadov proceeded therefore to a compression of the streamwise coordinate and took the scale for x as κ times the scale for y, hence the change $x = \kappa h_{\rm N}\tilde{x}$. Scaling time as $t = (\kappa/h_{\rm N})\tilde{t}$ and velocity components as $u = h_{\rm N}^2\tilde{u}$ and $v = (h_{\rm N}^2/\kappa)\tilde{v}$, dropping tildes, from (9) and (12) we get the rescaled equations as:

$$\delta\left(\partial_t u + u\partial_x u + v\partial_y u\right) = 1 + \partial_{yy}u - \zeta\partial_x h + \partial_{xxx}h + \eta\left(2\partial_{xx}u + \partial_x\left[\partial_x u|_h\right]\right), \tag{14}$$

and

$$\partial_y u|_h = \eta\left(4\partial_x h\partial_x u|_h - \partial_x v|_h\right) \,, \tag{15}$$

where

$$\delta = h_{\rm N}^3/\kappa = 3R\,W^{-1/3} \tag{16}$$

is a reduced Reynolds number. The two other reduced parameters

$$\zeta = B/\kappa = \cot\beta\, W^{-1/3} \qquad \text{and} \qquad \eta = \kappa^{-2} = W^{-2/3} \tag{17}$$

correspond to the effect of the gravity component normal to the plane and to the viscous second-order effects, respectively. The reduced Reynolds number introduced by Shkadov was $\delta/45$; the present choice is preferred since it leaves all numerical coefficients in the equations unchanged.
The set of reduced parameters δ, ζ and η is formally equivalent to the set R, B and W (or $h_{\rm N}$, B, Γ). However, an advantage of Shkadov's scaling is the gathering of all viscous dispersive terms under parameter η. Since these terms are the only physical ones of order ϵ^2 in equations (14,15), the truncation of these equations at first order leaves δ as the only parameter provided that the wall is vertical ($\zeta = 0$), as was the case in many studies. Direct numerical simulations (DNS) by Salamon *et al.* (1994) have however shown that second-order viscous dissipation effects do modify significantly the phase portrait of the traveling-wave families. As a matter of fact, though attributing the observed changes in the solutions to surface tension effects, they worked at constant reduced Reynolds number δ while changing the value of η. The observed modifications were therefore due to a larger momentum diffusion. Accordingly, improvement over the simple assumption $\eta = 0$ can further be expected by making use of equations (14,15). Considering terms in η as perturbations is a reasonable approach valid every time the surface tension is sufficiently large to ensure the separation of scales sustaining the whole approach (κ large). In fact, solitary waves turn out to be little sensitive to the value of η: the speed and amplitude of the solitary hump seem to be mostly controlled by the reduced Reynolds number δ (compare fig. 16 and 18 in Salamon *et al.* (1994)).

3 One-equation modeling

3.1 Gradient expansion and Benney's equation

Within our basic assumptions, the boundary-layer equations (8–12) are consistent at order ϵ^2. They can thus be viewed as the first step towards the modeling of film flows, i.e. the transformation of the basic equations into a set of equations of reduced complexity and/or dimensionality which capture the phenomena at stake as closely as possible.
Performing a gradient expansion of the basic equations or the boundary-layer equations (3, 8–11) leads to identical results up to order ϵ^2. Such an expansion of the basic equations was first done by Benney (1966) and next completed by Lin (1974) and Nakaya (1975). Benney showed that the velocity field $\mathbf{u}$ can be written as a series of polynomials in y, *i.e.* $\mathbf{u} = \sum_n \mathbf{A}_n(h) P_n(y)$, where the coefficients $\mathbf{A}_n$ are functions of the thickness h and its space-time derivatives, meaning that, in this limit, the velocity field is completely enslaved to the dynamics of h. Integration of the continuity equation (8) across the layer leads to the exact mass balance equation:

$$\partial_t h + \partial_x q = 0\,, \tag{18}$$

where $q = \int_0^h u\,\mathrm{d}y$ is the local flow rate. The gradient expansion of the momentum balance equation next gives an approximate expression for the flow rate as function of h and its derivatives:

$$q = q^{(0)}+q^{(1)} = \tfrac{1}{3}h^3-\delta\left(\tfrac{5}{24}h^4\partial_t h + \tfrac{3}{40}h^6\partial_x h\right)-\tfrac{1}{3}\zeta h^3\partial_x h+\tfrac{1}{3}h^3\partial_{xxx}h+O(\epsilon^2)\,, \tag{19}$$

where the contribution of the surface tension has been kept though it is formally of third order for the reasons discussed at length above.
Substituting (19) into (18) yields an evolution equation for the thickness:

$$\partial_t h+\tfrac{1}{3}\partial_x\left\{h^3-\tfrac{1}{8}\delta\,\partial_t(h^5)-\tfrac{9}{280}\delta\partial_x(h^7)-\tfrac{1}{4}\zeta\partial_x(h^4)+h^3\partial_{xxx}h\right\}=0\,. \tag{20}$$

This equation can be further simplified by using the zeroth-order relation $q^{(0)} = \frac{1}{3}h^3$ to exchange the time derivative of h against its space derivative through:

$$\partial_t h = -h^2\partial_x h\,, \tag{21}$$

which is the equation governing kinematic waves at the interface (Whitham, 1974). Following Benney, Gjevik thus studied the following equation (Gjevik, 1970, 1971):

$$\partial_t h + \tfrac{1}{3}\partial_x\left\{h^3+\tfrac{2}{35}\delta\partial_x(h^7)-\tfrac{1}{4}\zeta\partial_x(h^4)+h^3\partial_{xxx}h\right\}=0\,. \tag{22}$$

now known as the Benney equation. The relevance of this equation beyond a narrow neighborhood of the threshold is first limited by the fact that linear stability properties of the flat film solution rapidly depart from those derived from the exact Orr-Sommerfeld (OS) equation, *i.e.* the range of unstable wavenumbers predicted by (22) is much wider than that emerging from the solution of the OS equation.
This first limitation seems related to the neglect of the second-order streamwise dissipative terms as shown by Panga & Balakotaiah (2003). In fact Lin (1974) extended (22) to second order by including

$$q^{(2)} = \delta^2\left[\tfrac{127}{315}h^9(\partial_x h)^2+\tfrac{4}{63}h^{10}\partial_{xx}h\right]-\delta\zeta\left[\tfrac{8}{15}h^6(\partial_x h)^2+\tfrac{10}{63}h^7\partial_{xx}h\right] +\eta\left[\tfrac{7}{3}h^3(\partial_x h)^2+h^4\partial_{xx}h\right], \tag{23}$$

which completes (19) and makes these terms apparent under parameter η. Keeping only them into account, Panga and Balakotaiah obtained an equation which, within current scalings, reads:

$$\partial_t h+\tfrac{1}{3}\partial_x\left\{h^3-\tfrac{1}{8}\delta\,\partial_t(h^5)-\tfrac{9}{280}\delta\partial_x(h^7)-\tfrac{1}{4}\zeta\partial_x(h^4)+h^3\partial_{xxx}h +\eta\left[3h^4\partial_{xx}h+7h^3(\partial_x h)^2\right]\right\} = 0 \tag{24}$$

They were next able to prove that the exact OS results are recovered with better accuracy than by exchanging time and space derivatives of h through (21). Unfortunately, this correction does not cure the second well known limitation of the Benney equation (22), that is, the existence of finite-time blow up of solitary wave solutions beyond some limiting value of the Reynolds number not far beyond threshold (Pumir *et al.*, 1983; Scheid *et al.*, 2005*b*) since (24) also suffers from finite-time blow up of solutions somewhat beyond threshold (Ruyer-Quil & Manneville, 2004).

3.2 Regularization *à la* Padé

The Benney equation is indeed well known for the singular behavior of its solutions when the reduced Reynolds number δ becomes large enough. Pumir *et al.* (1983) showed in particular that the finite-time blow-up of time-dependent solutions closely corresponds to the loss of one-hump solitary waves, *i.e. homoclinic* orbits in the terminology of the dynamical systems theory. This suggests us that such a loss of what is called the 'principal homoclinic orbit' by Glendinning & Sparrow (1984) is accompanied with a blow-up of time-dependent solutions (Scheid *et al.*, 2005*b*), the trace of which —spontaneous formation of dry patches— can apparently not be found in experiments in the range of parameters currently explored. This unphysical feature has thus to be attributed to the assumptions underlying the derivation of the equations under study, either (22) or (24), and is likely related to the high degree of the inertia terms, especially the one of highest degree in h, $\frac{2}{105}\delta\partial_{xx}(h^7)$.

In order to remedy to this deficiency, Ooshida (1999) developed a resummation technique inspired from the Padé approximant technique. This technique relies on the idea that the divergence of a power series $Q=\sum_k Q_k x^k$ is due to the hidden presence of poles. This leads one to express Q in an approximate way as a ratio F/G of polynomials F and G where the zeros of G are supposed to capture the causes of the divergence. Adjusting the coefficients introduced in $F=F_0+F_1x+F_2x^2\ldots$ and $G=1+G_1x+G_2x^2+\ldots$ so that the terms in the series Q are reproduced exactly up to some given degree is the essence of the approximation, the ratio F/G being used in place of Q. In this conventional algebraic implementation, the degrees of the polynomials F and G are open to free choice, the number of coefficients to be determined staying compatible with the number of coefficients available in the series Q.

Ooshida translated this idea to the present case by introducing a regularization operator $\mathcal{G}=\mathcal{I}+\mathcal{G}^{(1)}+\mathcal{G}^{(2)}$, where $\mathcal{I}$ is the identity, $\mathcal{G}^{(1)}=G^{(1)}(h)\partial_x$, and $\mathcal{G}^{(2)}=G^{(2)}(h)\partial_{xx}$, so that the expansion of q as a function of h and its derivatives from the long wave expansion, formally written as $q\equiv\mathcal{Q}(h)$, is rewritten as $\mathcal{G}^{-1}\mathcal{F}$. Before presenting Ooshida's result at second order, let us implement this idea at first order since the singular behavior to be corrected is already present in (22). Here this simply comes to choose $\mathcal{G}$ in the form $\mathcal{I}+G^{(1)}(h)\partial_x$ with $G^{(1)}(h)$ to be determined so as to kill the dangerous terms in $\mathcal{F}$ when evaluating $\mathcal{G}\mathcal{Q}$. The explicit computation yields:

$$(\mathcal{I}+G^{(1)}\partial_x)\left[\tfrac{1}{3}\left(h^3+\delta\tfrac{2}{35}\partial_x(h^7)-\zeta\tfrac{1}{4}\partial_x(h^4)+h^3\partial_{xxx}h\right)\right]=$$
$$\tfrac{1}{3}\left[h^3+3h^2G^{(1)}\partial_x h+\delta\tfrac{2}{35}\partial_x(h^7)-\zeta\tfrac{1}{4}\partial_x(h^4)+h^3\partial_{xxx}h\right]+O(\epsilon^2)\,. \quad (25)$$

where $G^{(1)}$ is adjusted to $-\frac{2}{15}\delta\,h^4$ so that the term in factor of δ disappears on the r.h.s. of (25). Computing the regularized identity $\partial_x(\mathcal{G}\mathcal{Q})=\partial_x\mathcal{F}$ then gives:

$$\partial_x\mathcal{Q}-\partial_x\left[\tfrac{2}{15}\delta\,h^4\partial_x\mathcal{Q}\right]=\tfrac{1}{3}\partial_x\left[h^3-\zeta\tfrac{1}{4}\partial_x(h^4)+h^3\partial_{xxx}h\right]\,.$$

Replacing $\partial_x\mathcal{Q}$ by $-\partial_t h$ [from (18)] wherever it appears, we get:

$$\partial_t h+\tfrac{1}{3}\partial_x\left\{h^3-\tfrac{2}{25}\delta\,\partial_t(h^5)-\tfrac{1}{4}\zeta\partial_x(h^4)+h^3\partial_{xxx}h\right\}=0\,. \quad (26)$$

Working at second order, Ooshida chose rather to adjust "coefficients" $\mathcal{G}^{(1)}$ and $\mathcal{G}^{(2)}$ in $\mathcal{G}$ so that $\mathcal{G}\mathcal{Q} = \mathcal{F}$ could be reduced to $q^{(0)} + \mathcal{F}^{(1)}$, *i.e.* $\mathcal{F}^{(2)} \equiv 0$, which yielded:

$$\mathcal{G} = 1 - \tfrac{10}{21}\delta h^4 \partial_x - \eta h^2 \partial_{xx}\,.$$

Computation of the regularized identity $\partial_x(\mathcal{G}\mathcal{Q}) \equiv \partial_x \mathcal{F}$ with the replacement of $\partial_x \mathcal{Q}$ by $-\partial_t h$ led Ooshida to the equation:

$$\partial_t h + \tfrac{1}{3}\partial_x \left\{ h^3 - \tfrac{2}{7}\delta\, \partial_t(h^5) - \tfrac{36}{245}\delta \partial_x(h^7) - \tfrac{1}{4}\zeta \partial_x(h^4) + h^3 \partial_{xxx} h \right. \\ \left. -3\eta\, h^2 \partial_{xt} h \right\} = 0\,. \qquad (27)$$

3.3 Comparison of the different one-equation models

The main difference between Equations (20, 22, 26, 27) is that the inertia terms issued from $q^{(1)}$ appear as combinations of $\partial_t(h^5)$ and $\partial_x(h^7)$ with different weights. Indeed using with the equivalence $\partial_t h = -h^2 \partial_x h + O(\epsilon^2)$ one can write

$$h^6 \partial_x h = \partial_x \left(\tfrac{1}{7} h^7\right) = -\partial_t \left(\tfrac{1}{5} h^5\right) + O(\epsilon^2)\,. \qquad (28)$$

Thus let us investigate every equivalent combination of $\partial_t(h^5)$ and $\partial_x(h^7)$ when viscous effects can be neglected ($\eta = 0$), and thus consider

$$\partial_t h + \tfrac{1}{3}\partial_x \left\{ h^3 - \tfrac{2}{25}\delta\Delta \partial_t(h^5) - \tfrac{2}{35}\delta(\Delta - 1)\partial_x(h^7) - \tfrac{1}{4}\zeta \partial_x(h^4) + h^3 \partial_{xxx} h \right\} = 0\,, \qquad (29)$$

where Δ is a free parameter, as a starting point. The Benney equation (22) is clearly recovered when $\Delta = 0$ whereas (20) is obtained for $\Delta = 25/16 \simeq 1.7$. The combination of the first-order terms $\partial_t(h^5)$ and $\partial_x(h^7)$ appearing in Ooshida's equation (27) corresponds to $\Delta = 25/7 \simeq 3.6$ and Equation (26) is recovered when $\Delta = 1$. Figure 2 (left) displays the speeds of one-hump solitary waves as functions of the reduced Reynolds number δ for the corresponding values of parameter Δ. These solutions have been computed by continuation, again using AUTO97. It can be seen that the solution branches for the principal homoclinic orbits of the Benney equation (22) —dotted line— and equation (20) —dashed line— both present a turning point at $\delta \approx 1$, so that one-hump solitary solutions are not expected beyond the corresponding values of δ. The curve corresponding to $\Delta = 1$, i.e. Equation (26), is not shown in figure 2 since it remains close to the ones obtained with $\Delta = 0$ and $\Delta = 25/16$ and similarly presents a turning point. By contrast when $\Delta = 25/7$ —thick solid line— the curve does not turn back as δ is increased. Equation (29) with $\Delta = 25/7$ differs from Ooshida's equation (27) only through the absence of the viscous term $-\eta\partial_x(h^2\partial_{xt}h)$. However this viscous contribution does not play a significant role in the regularization process. Comparisons bearing on the existence and speed of the solitary waves (thick and thin solid lines in figure 2, left) indeed show little difference. Viscous dispersion does not affect much the maximum amplitude of the waves, whereas for $\eta = 0.1$ it has a marked effect on the overall shape of the wave's envelope and the number of visible oscillations preceding the main hump as seen in the right-hand-side part of figure 2. As long as the regularization of the surface equation is concerned, which manifests

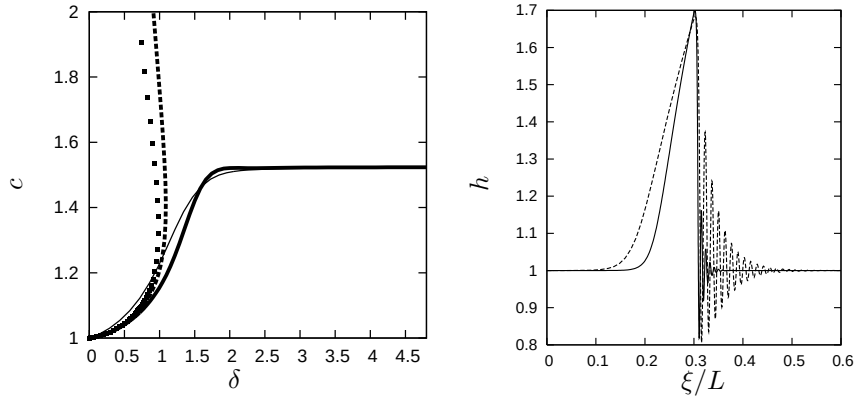

Figure 2: Left: Speeds of one-hump homoclinic solutions of (29) as functions of the reduced Reynolds number δ for a vertical wall ($\zeta = 0$). The dotted line stands for $\Delta = 0$. The dashed line corresponds to $\Delta = 25/16$ and the solid line to $\Delta = 25/7$. For comparison, the solutions to Ooshida's equation (27) with $\eta = 0.1$ are given as the thin solid line. Right: One-hump homoclinic solutions to Ooshida's equation (29) at $\delta = 5$ and $\zeta = 0$ (vertical wall); the solid line corresponds to $\eta = 0.1$ and the dotted line to $\eta = 0$.

itself through the persistence of homoclinic solutions for all Reynolds numbers, the computation of homoclinic solutions to (29) shows that it can be achieved without much algebra simply by modifying the inertia terms entering that equation with the help of the equivalence $\partial_t h = -h^2\partial_x h + O(\epsilon^2)$. Unfortunately, this is not sufficient to obtain quantitative agreement with experiments and DNS results. As already recognized by Ooshida (1999), the amplitudes of solitary waves are indeed grossly underestimated by (27). The same problem arises with (29) for all the values of Δ that we have explored besides the special values previously quoted. This calls for a different approach if we want an accurate modeling in the largest possible range of Reynolds numbers and not only in the neighborhood of the instability threshold, i.e. also in what Ooshida called the 'drag-inertia' regime that takes place when inertia plays a more significant role at large δ, as opposed to the 'drag-gravity' regime taking place at small δ and corresponding to a balance between viscous drag on the wall and gravity acceleration, for which the classical long-wavelength expansion is expected to be valid.

4 Shkadov's modeling and beyond

4.1 Original Shkadov's approach

The difficulty with a modeling in terms of a single equation, is that keeping a single dependent variable, namely h, is not enough to account for the dynamics of the film, though the perturbations may well stay long-lengthed.

At every step of the asymptotic expansion, the velocity profile is assumed to have no dynamics for its own but to be strictly enslaved to h by equations where the time dependence only comes through that of h. This is justified only as long as the evolution rate of velocity modes, of order unity due to the viscous damping over the thickness, can be considered as large when compared to the evolution rate of h, of order ϵ. Beyond threshold (ϵ finite) this assumption fails, which can be interpreted as the sign of a revolt of enslaved degrees of freedom. The dynamics of the flow can then no longer be described through the evolution of a single field for the film thickness and other variables must be considered, *e.g.* the local flow rate q, the stress at the wall, *etc.*

Kapitza (1948) first proposed a modeling involving the film thickness h and the flow rate q, based on the Kármán–Polhausen averaging technique used in laminar boundary-layer theory (Schlichting, 1979). Extending Kapitza's theory to time-dependent flows, within a similarity assumption based on a parabolic velocity profile:

$$u = \frac{3q}{h}\left[\bar{y} - \frac{1}{2}\bar{y}^2\right] \qquad \text{where} \qquad \bar{y} = y/h(x,t)\,, \tag{30}$$

Shkadov (1967) obtained an equation governing the flow rate q which, using the previously defined scales, reads:

$$\delta\,\partial_t q = h - 3\frac{q}{h^2} + \delta\left[\frac{6}{5}\frac{q^2}{h^2}\partial_x h - \frac{12}{5}\frac{q}{h}\partial_x q\right] - \zeta h\partial_x h + h\partial_{xxx}h\,. \tag{31}$$

This equation forms a closed system when completed by the mass conservation equation (18). The blow-up behavior observed with the time-dependent solutions of the Benney equation is no longer observed with the two-equation model (18, 31), but the linear stability analysis of that system leads to an overestimation of the threshold of instability ($\cot\beta$ instead of the exact answer $\frac{5}{6}\cot\beta$). This discrepancy motivated Ruyer-Quil & Manneville (2000) to re-investigate Shkadov's approach and pursue his original suggestion of expanding the velocity field on a polynomial basis as $\mathbf{u} = \sum_n \mathbf{a}_n(x,t) f_n(y/h(x,t))$. They were lead to a system consistent at order ϵ^2, with four equations in four unknowns, h, q and two supplementary fields s_1 and s_2 accounting for the departure of the velocity profile from the parabolic shape.

4.2 Full second-order model

The main idea underlying the derivation of this second-order model was to take advantage of the structure of (9) which can be understood as a perturbation, by inertia terms and streamwise viscous dissipation, of the equilibrium between the streamwise gravity and wall friction represented by its $O(1)$ restriction, namely: $1+\partial_{yy}u = 0$. Consequently, the velocity profile is expected to remain close to the corresponding unperturbed solution: the flat film Nusselt flow. Expanding the velocity field on a polynomial basis, the first term of this expansion was taken to be $g_0(y) = y - \frac{1}{2}y^2$, the flat film parabolic velocity profile as in (30). It was proved that first-order corrections

to the velocity fields could be described entirely with the help of only two more polynomials of degree four and six, g_1 and g_2. We next proceeded to a Galerkin projection of the boundary-layer equations (14) retaining terms up to order ϵ^2 included. Writing formally (14) as $BL(u) = 0$, the residuals read $\mathcal{R}_i(u) = \langle BL(u),\, g_i(y)\rangle$, where $\langle f,\, g\rangle = \int_0^h f\, g\, \mathrm{d}y$ refers to the scalar product deriving from the plain $\mathcal{L}^2$ norm. In practice, the actual set of polynomial test functions g_i was made orthogonal. The expansion of the velocity field was also written so as to retain the physical meaning of q as the flow rate, i.e. $q = \int_0^h u\, \mathrm{d}y$. Setting the three residuals $\mathcal{R}_i(u)$ to zero formed a system of three equations, completed with the mass balance (18), for the four unknown h, q, s_1 and s_2. The full second-order model was obtained after tedious algebra as:

$$\delta\, \partial_t \mathbf{U} = \mathbf{M}\, \mathbf{V} + \delta\, \mathbf{M}_\delta\, \mathbf{V}_\delta + \eta\, \mathbf{M}_\eta\, \mathbf{V}_\eta\,, \tag{32}$$

again completed by (18) and where $\mathbf{U}$ is the column vector $\mathbf{U} = (q, s_1, s_2)^t$. The full expression of system (32) is given in appendix A, from which the arrays $\mathbf{M}$, $\mathbf{M}_\delta$, and $\mathbf{M}_\eta$ as well as $\mathbf{V}$, $\mathbf{V}_\delta$, and $\mathbf{V}_\eta$, can be read. Once closed with the mass conservation equation (18), this model was shown to reproduce the dynamics of the film with great accuracy up to large Reynolds numbers. In particular, linear stability predictions were found in close agreement with results from the OS equation obtained by Brevdo *et al.* (1999) at least up to $R = 200$ (Ruyer-Quil & Manneville, 2002).

4.3 Simplified second-order model

Application of the Galerkin procedure with a single test function g_0, that is assuming the parabolic velocity profile given by (30), yielded a simplified model involving h and q:

$$\begin{aligned}\delta\, \partial_t q \;=\;& \frac{5}{6}h - \frac{5}{2}\frac{q}{h^2} + \delta\left[\frac{9}{7}\frac{q^2}{h^2}\partial_x h - \frac{17}{7}\frac{q}{h}\partial_x q\right] - \frac{5}{6}\zeta h\partial_x h + \frac{5}{6}h\partial_{xxx}h \\ &+\eta\left[4\frac{q}{h^2}(\partial_x h)^2 - \frac{9}{2h}\partial_x q\partial_x h - 6\frac{q}{h}\partial_{xx}h + \frac{9}{2}\partial_{xx}q\right],\end{aligned} \tag{33}$$

i.e. similar to Shkadov's model once closed by (18). But, by contrast with the latter which was derived through simple averaging (y-constant weight function), our simplified model was shown to predict the correct linear stability threshold. It also contained all possible second order terms in h and q, which should make it more relevant also beyond threshold. The gradient expansion of (33) however failed to reproduce the exact expression (23) at order ϵ^2. As a matter of fact, results differ only through the coefficient of the first inertia term that reads $\frac{212}{525}$ instead of the exact value $\frac{127}{315}$.
There is a strong motivation in obtaining accurate second-order low-dimensional models only involving two equations for two independent variables such as h and q. The theoretical analysis and the numerical integration of models such as (18,32) are indeed simpler than the corresponding study of the full Navier–Stokes problem, or even of the boundary-layer formulation (9). Handling the four fields of (18,32) still remains a difficult task, and a reliable two-field formulation consistent at order ϵ^2 would be welcome, and all

the more when the spanwise uniform assumption will be relaxed in Part II. Elimination of s_1 and s_2 can be achieved starting from (32) and assuming them to be in practice of higher order than ϵ and therefore enslaved to the other degrees of freedom h and q. This procedure leads back to the simplified equation (33). We develop below a consistent elimination strategy aiming at a two-equation model with an exact account of the gradient expansion at order ϵ^2.

5 Reduction of the full second order model

A simple argument can be given here to justify the success of the elimination of s_1 and s_2. Since viscosity acts so as to ensure the in-depth coherence of the flow, fluctuations of the flow field varying rapidly in the wall-normal direction are efficiently damped by viscosity, so that s_1 and s_2 corresponding to high degree polynomials, should be efficiently damped by it. This can be observed simply by linearizing system (32) around the Nusselt flow in the zero wavenumber limit, that is, assuming no spatial variations. The mass balance (18) thus implies a constant thickness. Writing $q = 1/3 + \varepsilon\tilde{q}$, $s_i = \varepsilon\tilde{s}_i$ where $\varepsilon \ll 1$, we get

$$\delta \frac{d\tilde{\mathbf{V}}}{dt} = \mathbf{M}\,\tilde{\mathbf{V}}\,, \tag{34}$$

where $\tilde{\mathbf{V}} = (\tilde{q},\, \tilde{s_1},\, \tilde{s_2})^t$ and $\mathbf{M}$ is the matrix defined in (32) whose eigenvalues λ_i are respectively -2.47, -22.3, and -87.7. Because of the large gap between λ_1 and $(\lambda_2,\, \lambda_3)$, it is obvious that, at low Reynolds number and provided that the long-wave assumption is valid, the dynamics of the flow is governed by the neutral mode associated to the free surface elevation and the eigenmode corresponding to λ_1, the eigenvector of which is $(\tilde{q},\, \tilde{s_1},\, \tilde{s_2})^t = (1.00, -1.33\,10^{-2}, 1.38\,10^{-4})^t$. Consequently and given that the associated eigenvector is nearly aligned with the first vector of the natural basis, s_1 and s_2 are truly slaved to the dynamics of the thickness of flow rate, at least close to the threshold.

5.1 Technicalities

Having justified the elimination of s_1 and s_2, let us go back to its practical implementation. Fields s_1 and s_2 are corrections to the flat film parabolic profile corresponding to g_0. So, they are at least first-order terms produced by the deformation of the free surface. In the first residual $\mathcal{R}_0$ associated to the weight g_0, s_1 and s_2 appear through inertia terms involving their space and time derivatives or through products with derivatives of h and q, which are terms of order ϵ^2. Indeed, the corrections to the velocity field cannot appear in $\mathcal{R}_0$ at lowest order since the evaluation of the viscous term $\int_0^h g_0(y/h)\partial_{yy}u\,\mathrm{d}y$ yields $\frac{1}{2}\partial_y u|_{y=h} - q/h^2$, owing to the definition of $q = \int_0^h u\,\mathrm{d}y$, and that $\frac{1}{2}\partial_y u|_{y=h}$ is already of order ϵ^2, as seen from (12) that expresses the stress balance at the free surface.
At this stage, it remains to determine the expression of s_1 and s_2 as functions of h, q and their derivatives truncated at order ϵ. Such relations can easily

be obtained by dropping all second-order terms from the two last residuals $\mathcal{R}_1$ and $\mathcal{R}_2$ and then solving for s_1 and s_2. One gets :

$$s_1 = \delta\left[\frac{1}{210}h^2\partial_t q - \frac{19}{1925}q^2\partial_x h + \frac{74}{5775}hq\partial_x q\right] + O(\epsilon^2)\,, \quad (35a)$$

$$s_2 = \delta\left[\frac{2}{5775}q^2\partial_x h - \frac{2}{17325}hq\partial_x q\right] + O(\epsilon^2)\,. \quad (35b)$$

Substitution of (35) into $\mathcal{R}_0$ finally gives

$$\delta\,\partial_t q = \frac{5}{6}h - \frac{5}{2}\frac{q}{h^2} + \delta\left[\frac{9}{7}\frac{q^2}{h^2}\partial_x h - \frac{17}{7}\frac{q}{h}\partial_x q\right] + \delta^2\mathcal{K}(h,\,q) - \frac{5}{6}\zeta h\partial_x h + \eta\left[4\frac{q}{h^2}(\partial_x h)^2 - \frac{9}{2h}\partial_x q\partial_x h - 6\frac{q}{h}\partial_{xx}h + \frac{9}{2}\partial_{xx}q\right] + \frac{5}{6}h\partial_{xxx}h\,, \quad (36)$$

where the additional terms arising from the elimination of s_1 and s_2 are second order inertia terms all gathered in $\mathcal{K}$ that reads:

$$\mathcal{K} = \frac{1}{210}h^2\partial_{tt}q - \frac{1}{105}q\partial_x h\partial_t q + \frac{1}{42}h\partial_x q\partial_t q + \frac{17}{630}hq\partial_{xt}q + \frac{653}{8085}q\,(\partial_x q)^2 - \frac{26}{231}\frac{q^2}{h}\partial_x h\partial_x q + \frac{386}{8085}q^2\partial_{xx}q + \frac{104}{2695}\frac{q^3}{h^2}(\partial_x h)^2 - \frac{78}{2695}\frac{q^3}{h}\partial_{xx}h\,. \quad (37)$$

Obviously, these corrections are highly nonlinear. They also present time derivatives that are difficult to handle at least in numerical simulations. Fortunately, the zeroth-order relation between q and h

$$q = \frac{1}{3}h^3\,, \quad (38)$$

allows us to simplify the expression of $\mathcal{K}$. Using also $\partial_t h = -h^2\partial_x h + O(\epsilon^2)$, we get the more compact expression:

$$\mathcal{K} = -\frac{1}{630}h^7(\partial_x h)^2\,. \quad (39)$$

The behavior of the solutions to equation (36) where the inertia corrections $\mathcal{K}$ are given by (37) or (39) have been tested in the drag-inertia regime by computing the one-hump solitary-wave solutions for a vertical wall and neglecting second-order viscous effects ($\eta = 0$). Figure 3 displays the speed and amplitude of the solitary waves as function of the reduced Reynolds number δ. They are compared to the solutions to the full-second order model (32), to the simplified model (18, 33), and to the results obtained by Chang *et al.* (1996*a*) with the first-order boundary-layer equations [(8, 14), with (11, 15, 10) and $\eta = 0$]. The simplified model and the full second-order model both exhibit unique one-hump solitary-wave solutions at given δ and have speed in reasonable agreement with the results of Chang *et al.* On the contrary, the branch of principal homoclinic solutions is seen to turn back in the transition region between the drag-gravity and the drag-inertia regimes ($\delta \sim 1$) with both expressions (37) and (39) of $\mathcal{K}$. This unphysical behavior is similar to the one encountered with the Benney equation (22)

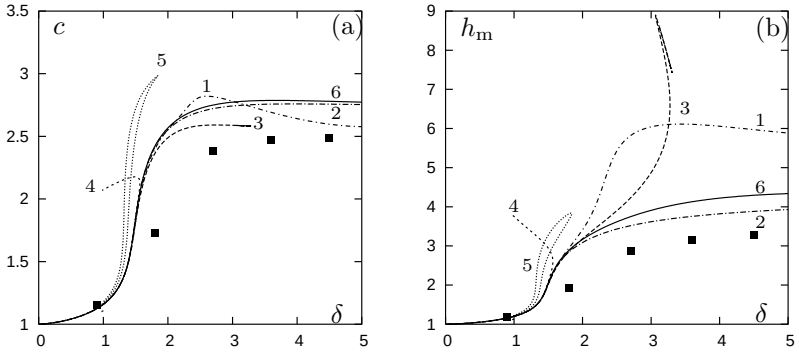

Figure 3: Speed c (a) and amplitude $h_{\rm m}$ (b) of the principal homoclinic orbits as functions of the reduced Reynolds number δ. The wall is vertical and streamwise viscous dissipation is omitted ($\zeta = \eta = 0$). 1: full second-order model (18,32); 2: simplified model (18,33); 3: (18, 36) with $\mathcal{K}$ given by (37); 4: with $\mathcal{K}$ given by (39); 5: with $\mathcal{K}$ given by (40); 6: regularized model (18, 47); filled squares: solutions to the first-order boundary-layer equations after Chang *et al.* (1996*a*).

and is likely to be related to the high-degree nonlinearities present in (37) and (39). We therefore end up with basically the same difficulty as in the case of surface equations (see § 3): obtain inertia terms in a form that accounts for the drag-inertia regime in a wider range of reduced Reynolds number δ accurately.

Other forms of the second-order inertia corrections $\mathcal{K}$ can be obtained by using the flat-film relation (38). For example, Roberts (1996) has applied a center manifold analysis to the problem of falling film and derived a second-order model in terms of the film thickness h and the depth-averaged velocity equivalent to the flow rate q. His approach relied on the linear viscous dissipating modes of the streamwise uniform film in the zero-wavenumber limit, which is basically a reduction of the slow time and space evolution of the film to the two first eigenmodes $(h,\, u) \propto (1,\, 0)$ and $(h,\, u) \propto (0, \sin(\pi y/(2h)))$. His model is similar to those obtained using the classical depth-averaged method with coefficients close to those appearing in (36). As noticed Ooshida (1999), this agreement can be understood from the fact that the velocity profile $u_{\rm rob} \propto \sin(\pi y/(2h))$ is very close to the parabolic profile since $\langle u_{\rm rob}, g_0\rangle / \sqrt{\langle u_{\rm rob}, u_{\rm rob}\rangle \langle g_0, g_0\rangle} \approx 0.999$. Inertia corrections obtained by Roberts read:

$$\mathcal{K} = \frac{1}{100}\left(-0.1961\,\frac{q^3}{h^2}(\partial_x h)^2 - 1.78\,\frac{q^2}{h}\partial_x h \partial_x q + 0.1226\, q(\partial_x q)^2 \right.$$
$$\left. -1.792\,\frac{q^3}{h}\partial_{xx} h + 0.7778\, q^2 \partial_{xx} q\right). \qquad (40)$$

The results obtained with this expression of $\mathcal{K}$ are also displayed in figure 3. A loss of solutions is once more observed at $\delta \approx 2$, a failure due to the

fact that $\mathcal{K}$ is obtained from a perturbation method which is strictly valid only in the drag-gravity regime where inertia has a perturbative role only. Both our derivation of (36) with $\mathcal{K}$ given by (37) or (39) are also based on perturbative techniques applied to the Nusselt flat film solution. However, the presence of the principal homoclinic solutions to the simplified model (18, 33) for all δ shows that it should be possible to describe the drag-inertia regime at low cost in terms of a model involving h and q only.

5.2 Padé-like regularization

Here, by looking for a kind of algebraic preconditioner apt to kill the dangerous second order terms of inertia origin (in δ^2), we follow a procedure more closely inspired from the Padé approximant technique than Ooshida's regularization that involved a differential operator. Instead of thinking in terms of an expansion of the flow rate q, let us consider the residual $\mathcal{R}_0$ obtained by averaging the momentum equation (14) with weight g_0, which can be written as a series in ϵ, $\mathcal{R}_0^{(0)}+\mathcal{R}_0^{(1)}+\mathcal{R}_0^{(2),\eta}+\mathcal{R}_0^{(2),\delta}$. In the second-order terms of this expansion, we have splitted those having a viscous origin (superscript η) from those accounting for the convective acceleration induced by the deviations of the velocity profile away from the parabolic shape (superscript δ). The simplified equation (33) is recovered just by neglecting $\mathcal{R}_0^{(2),\delta}$. So $\mathcal{R}_0$ is looked after in the form $\mathcal{G}^{-1}\mathcal{F}$ where $\mathcal{G}$ is now simply a function of h, q and their derivatives, and $\mathcal{F}$ is reduced to $\mathcal{R}_0^{(0)}+\mathcal{R}_0^{(1)}+\mathcal{R}_0^{(2),\eta}$, i.e. the residual that was obtained assuming a parabolic velocity profile. Setting $\mathcal{F}=\mathcal{G}\mathcal{R}_0$ to zero gives

$$\delta\,\mathcal{G}(h,q)\int_0^h g_0(y/h)\left[\partial_t u+u\partial_x u+v\partial_y u\right]\mathrm{d}y=$$
$$\mathcal{G}(h,q)\int_0^h g_0(y/h)\left\{1+\partial_{yy}u-\zeta\partial_x h+\partial_{xxx}h+\eta\left(2\partial_{xx}u+\partial_x\left[\partial_x u\big|_h\right]\right)\right\}\mathrm{d}y \quad (41)$$

where inertia terms have been isolated on the l.h.s. and read:

$$\delta\mathcal{G}\int_0^h g_0(y/h)\left[\partial_t u+u\partial_x u+v\partial_y u\right]\mathrm{d}y=$$
$$\delta\mathcal{G}\left\{\left[\frac{2}{5}\partial_t q-\frac{18}{35}\frac{q^2}{h^2}\partial_x h+\frac{34}{35}\frac{q}{h}\partial_x q\right]-\frac{2}{5}\delta\mathcal{K}\right\}\equiv\mathcal{G}\left\{\mathcal{R}_0^{(1),\delta}+\mathcal{R}_0^{(2),\delta}\right\} \quad (42)$$

which we want to identify to:

$$\delta\left[\frac{2}{5}\partial_t q-\frac{18}{35}\frac{q^2}{h^2}\partial_x h+\frac{34}{35}\frac{q}{h}\partial_x q\right]\equiv\mathcal{R}_0^{(1),\delta}\,. \quad (43)$$

This leads to take the regularization factor as:

$$\mathcal{G}=\left[1+\frac{\mathcal{R}_0^{(2),\delta}}{\mathcal{R}_0^{(1),\delta}}\right]^{-1}\,. \quad (44)$$

An asymptotically equivalent expression of $\mathcal{G}$ can be found using $q = h^3/3 + O(\epsilon)$, and $\partial_t h = -h^2\partial_x h + O(\epsilon^2)$. We then obtain:

$$\mathcal{R}_0^{(1),\delta} = -\frac{2}{15}\delta h^4 \partial_x h + O(\epsilon^2) \qquad \text{and} \qquad \mathcal{R}_0^{(2),\delta} = \frac{\delta^2}{1575} h^7 (\partial_x h)^2 + O(\epsilon^3)\,,$$

which, when substituted in (44), yields:

$$\mathcal{G} = \left[1 - \frac{\delta}{210} h^3 \partial_x h\right]^{-1} + O(\epsilon^2)\,, \tag{45}$$

In order to lower at its maximum the degree of nonlinearities, $\mathcal{G}$ is finally rewritten in terms of the local slope $\partial_x h$ and the local Reynolds number $\delta\, q$:

$$\mathcal{G} = \left[1 - \frac{\delta}{70} q \partial_x h\right]^{-1}\,. \tag{46}$$

The resulting set of equations reads:

$$\begin{aligned}
\delta\,\partial_t q \;=\;& \delta\left[\frac{9}{7}\frac{q^2}{h^2}\partial_x h - \frac{17}{7}\frac{q}{h}\partial_x q\right] \\
&+ \left\{\frac{5}{6}h - \frac{5}{2}\frac{q}{h^2} + \eta\left[4\frac{q}{h^2}(\partial_x h)^2 - \frac{9}{2h}\partial_x q \partial_x h - 6\frac{q}{h}\partial_{xx} h + \frac{9}{2}\partial_{xx} q\right]\right. \\
&\left. - \frac{5}{6}\zeta h \partial_x h + \frac{5}{6} h \partial_{xxx} h\right\} \times \left[1 - \frac{\delta}{70} q \partial_x h\right]^{-1}\,,
\end{aligned} \tag{47}$$

along with the mass balance equation (18).
Hereafter, the system (18, 47) will be referred to as the *regularized model*. Homoclinic orbits corresponding to one-hump solitary-wave solutions to (18, 47) have been computed and are displayed as curves labelled 6 in figure 3. Non-physical turn-backs of the curves have never been observed for all the values of δ studied. Moreover, system (18, 47) is fully consistent at second-order with the Benney expansion and takes into account modifications of the momentum balance of the film induced by the deviations of the velocity profile from the parabolic Nusselt solution.
Note that computations of 2D waves have shown few differences between the *simplified* and the *regularized* models, at least in the range of parameters corresponding to available experimental data. For this reason, we will pass directly to the second Part of these lecture notes where the regularized model is extended to account for spanwise modulations of the film surface, the selection of which will be shown to be strongly influenced by the second-order inertia effects. For results of 2D waves with the *simplified* model, the reader is referred to the lecture notes of Christian Ruyer-Quil.

Part II
Secondary Instability and 3D Wave Patterns

6 2D modeling of 3D film flows

We now turn to the 3D formulation of the problem, and look for two-dimensional equations in the streamwise (x) and spanwise (z) coordinates for quantities averaged over cross-stream coordinate y that mimic the full 3D motion of the fluid. As in Part I, our approach is based on the long-wave approximation which ensures slow time and space modulations of the basic flat film solution, called the Nusselt flow, by writing that partial derivatives $\partial_t, \partial_x, \partial_z$ are all of order ϵ, with $\epsilon \ll 1$. The first step to this approximation consists in the elimination of the pressure in the Navier–Stokes equations truncated at $O(\epsilon^3)$, leading to the second-order boundary layer equations, which read

$$\delta\left[\partial_t u + \partial_x(u^2) + \partial_y(uv) + \partial_z(uw)\right] = 1 + \partial_{yy}u - \zeta\,\partial_x h + \partial_{xxx}h + \partial_{xzz}h + \eta\left[2\partial_{xx}u + \partial_{zz}u + \partial_{xz}w - \partial_x(\partial_y v\big|_h)\right], \tag{48a}$$

$$\delta\left[\partial_t w + \partial_x(uw) + \partial_y(vw) + \partial_z(w^2)\right] = \partial_{yy}w - \zeta\,\partial_z h + \partial_{xxz}h + \partial_{zzz}h + \eta\left[2\partial_{zz}w + \partial_{xx}w + \partial_{xz}u - \partial_z(\partial_y v\big|_h)\right], \tag{48b}$$

$$\partial_x u + \partial_y v + \partial_z w = 0\,, \tag{48c}$$

where $h = h(x, z, t)$ is the local film thickness, and (u, v, w) the streamwise, cross-stream and spanwise components of the velocity field. Equations (48a) and (48b) correspond to the streamwise and spanwise momentum balances, respectively, and (48c) is the continuity equation. This set of equations is completed by the no-slip condition at the wall (at $y = 0$):

$$u = v = w = 0\,, \tag{48d}$$

and the projections of the stress balance at the free surface (at $y = h$) along the x and z directions:

$$\partial_y u = \eta\left[\partial_z h(\partial_z u + \partial_x w) + 2\partial_x h(2\partial_x u + \partial_z w) - \partial_x v\right], \tag{48e}$$

$$\partial_y w = \eta\left[\partial_x h(\partial_z u + \partial_x w) + 2\partial_z h(2\partial_z w + \partial_x u) - \partial_z v\right]. \tag{48f}$$

The set of equations (48) has been written using Shkadov's scaling introduced in Part I. In this scaling, the length scale in the wall-normal direction y is $h_{\rm N}$, the length scale in the in-plane directions x and z and the time scale are respectively

$$h_{\rm N}W^{1/3} \quad \text{and} \quad \nu W^{1/3}/g\sin\beta h_{\rm N}\,. \tag{49}$$

Second-order terms gathered under η in system (48) account for streamwise viscous dispersion. These equations are symmetric under the exchanges

$\{u \leftrightarrow w,\, x \leftrightarrow z\}$, except for the gravity term equal to 1 in (48a). Gravity oriented, the trivial flat film solution is a parallel flow with no spanwise component, i.e. $w = 0$. A legitimate approach is therefore to consider w of order ϵ, with the meaning that spanwise flows are triggered by the modulations of the free surface. Ruyer-Quil & Manneville (2000) used this assumption to simplify cumbersome system of equations which models the 3D flow dynamics. However, considering the continuity equation (48c), the least degeneracy principle suggests that w be taken as an $O(1)$ quantity and this is the point of view we will consider below.

Following the same procedure as for the 2D case in Part I, one obtains that six fields are needed to represent the velocity components at second order: both the streamwise and spanwise flow rates $q = \int_0^h u\,\mathrm{d}y$ and $p = \int_0^h w\,\mathrm{d}y$, and four corrections s_1, s_2, r_1 and r_2 corresponding to the polynomial test functions g_1 and g_2 and accounting for the deviations of the velocity profiles from their zeroth-order parabolic shapes (polynomial g_0): see details in appendix B. The boundary layer equations are next averaged using the Galerkin method by writing residuals $\langle E_\parallel, g_i\rangle$ and $\langle E_\perp, g_i\rangle$ where $\langle f, g\rangle = \int_0^h f\,g\,\mathrm{d}y$, and $E_\parallel$ and $E_\perp$ refer to the streamwise (48a) and spanwise (48b) momentum balances, respectively. These residuals yield a system of six evolution equations for h, q, s_1, s_2, p, r_1 and r_2, completed by the mass balance obtained through in-depth integration of (48c). This system is called the *complete model* in the following, and is given in appendix B for reference. Here, we follow the regularization procedure developed in Part I that aims at reducing the system to only three equations for h, q and p. First-order expressions of the corrective fields s_1, s_2, r_1 and r_2 are readily obtained from the truncation at order ϵ of the residuals corresponding to the weights g_1 and g_2. Substitution of these expressions in the first residuals $\mathcal{R}_{0,\parallel} = \langle E_\parallel, g_0\rangle$ and $\mathcal{R}_{0,\perp} = \langle E_\perp, g_0\rangle$ produces second-order inertia terms, formally written $\mathcal{R}_{0,\parallel}^{(2),\delta}$ and $\mathcal{R}_{0,\perp}^{(2),\delta}$. These terms contain dangerous nonlinearities that we next kill by adjusting algebraic preconditioners. So residuals $\mathcal{R}_{0,\parallel}$ and $\mathcal{R}_{0,\perp}$ are searched in the form $\mathcal{G}_\parallel^{-1}\mathcal{F}_\parallel$ and $\mathcal{G}_\perp^{-1}\mathcal{F}_\perp$ where $\mathcal{F}_\parallel$ and $\mathcal{F}_\perp$ correspond to the expressions of the residuals $\mathcal{R}_{0,\parallel}$ and $\mathcal{R}_{0,\perp}$ when a parabolic velocity profile is assumed, i.e. when corrections s_i and r_i are neglected. Isolating inertia terms, we thus set:

$$\mathcal{G}_\parallel\left(\mathcal{R}_{0,\parallel}^{(1),\delta} + \mathcal{R}_{0,\parallel}^{(2),\delta}\right) = \mathcal{R}_{0,\parallel}^{(1),\delta} \quad \text{and} \quad \mathcal{G}_\perp\left(\mathcal{R}_{0,\perp}^{(1),\delta} + \mathcal{R}_{0,\perp}^{(2),\delta}\right) = \mathcal{R}_{0,\perp}^{(1),\delta}\,, \quad (50)$$

where superscripts refer to first-order and second-order inertia terms. Zeroth-order expressions of the flow rates $q = h^3/3 + O(\epsilon)$ and $p = O(\epsilon)$, i.e. the gravity-oriented Nusselt flow, are next invoked to reduce the degree of nonlinearities of the regularization factors $\mathcal{G}_\parallel$ and $\mathcal{G}_\perp$. Consequently, the inertia terms $\mathcal{R}_{0,\perp}^{(2),\delta}$ induced by deviations of the spanwise velocity field from the parabolic profile appearing asymptotically at order ϵ^3, we merely get $\mathcal{G}_\perp = 1 + O(\epsilon^2)$. Similarly, the asymptotic expression of $\mathcal{R}_{0,\parallel}^{(2),\delta}$ corresponds exactly to the one obtained for a spanwise independent flow. Hence we have

$$\mathcal{G}_\perp \equiv 1 \quad \text{and} \quad \mathcal{G}_\parallel \equiv \left[1 - \frac{\delta}{70} q \partial_x h\right]^{-1}\,, \quad (51)$$

where $\mathcal{G}_\parallel$ is identical to its expression given in Part I. The three-dimensional extension of our *regularized model* finally reads:

$$\partial_t h = -\partial_x q - \partial_z p\,, \tag{52a}$$

$$\delta\,\partial_t q = \delta\,\mathcal{I}_\parallel^{2D} + \mathcal{G}_\parallel \left\{ \frac{5}{6}h - \frac{5}{2}\frac{q}{h^2} + \delta\,\mathcal{I}_\parallel^{3D} + \eta\left[\mathcal{D}_\parallel^{2D} + \mathcal{D}_\parallel^{3D}\right] + \frac{5}{6}h\partial_x\mathcal{P} \right\}, \tag{52b}$$

$$\delta\,\partial_t p = \delta\,\mathcal{I}_\perp^{2D} - \frac{5}{2}\frac{p}{h^2} + \delta\,\mathcal{I}_\perp^{3D} + \eta\left[\mathcal{D}_\perp^{2D} + \mathcal{D}_\perp^{3D}\right] + \frac{5}{6}h\partial_z\mathcal{P}\,, \tag{52c}$$

where $\mathcal{I}$ and $\mathcal{D}$ stand for terms of inertia and viscous dispersion origin, and $\mathcal{P} = -\zeta h + (\partial_{xx} + \partial_{zz})h$ corresponds to contributions from gravity and capillarity to the pressure distribution. In (52b), we have also isolated terms already present in the 2D model (superscript $2D$) from those arising from the spanwise dependence (superscript 3D). Subscripts $\parallel$ and $\perp$ indicates terms that are symmetric under the exchanges $\{q \leftrightarrow p,\, x \leftrightarrow z\}$. Developed expressions of system (52) is given in appendix C.

Equations (52a) express the mass conservation, and (52b,52c) express the averaged momentum balances in directions x and z, respectively. The viscous drag corresponds to the terms $\frac{5}{2}q/h^2$ in (52b) and $\frac{5}{2}p/h^2$ in (52c). As for system (48), gravity acceleration contributes only to the streamwise momentum balance through the term $\frac{5}{6}h$ in (52b).

Regularized model (52) is fully consistent with the Benney expansion at second order, while the 3D *simplified model*, corresponding to the in-depth averaging of the momentum balance equations assuming both parabolic velocity profiles and weights, is not. The latter can be recovered from the former by replacing the factor $\mathcal{G}_\parallel$ by one[†] —or equivalently by assuming the actual order of s_i, r_i to be higher than ϵ, so that their derivatives can be neglected in the *complete model* (63) (Ruyer-Quil & Manneville, 2000).

7 Floquet Analysis

In this section, the stability of 2D waves against transverse perturbations is investigated, with a particular attention paid to the experimental conditions considered by Liu *et al.* (1995). Imposing a periodic forcing at the inlet, Liu *et al.* observed waves with the same periodicity in time, at least prior to the onset of secondary instabilities. Integrating the mass balance $\partial_t h + \partial_x q = 0$ over a period, shows that the mean flow rate $\langle q \rangle$ is conserved at each location on the plane, at least prior to secondary instabilities, and is therefore equal to its value 1/3 at inlet. Experimental profiles indicate that the wave selected by the linear inception are of type γ_1, slow waves with deep troughs and bumped crests. Our efforts have accordingly been concentrated on the stability analysis of the γ_1 traveling waves. These waves were computed using AUTO97 (Doedel *et al.*, 1997) by continuation. The constant flux condition $\langle q \rangle = 1/3$ was enforced by adjusting the mean flow rate in the moving frame $q_0 = \int_0^h (u - c)\,\mathrm{d}y$ where c is the wave

[†]Notice that the simplified model formulated by Ruyer-Quil & Manneville (2000) contains two typing mistakes in their equation (54): terms $-\frac{97}{56}q\partial_z p/h$ and $\frac{129}{56}qp\partial_z h/h^2$ must be corrected to read $-\frac{8}{7}q\partial_z p/h$ and $\frac{9}{7}qp\partial_z h/h^2$.

speed. We started from infinitesimal sinusoidal waves at linear threshold, and increased the period. A standard Floquet stability analysis of the wave against both streamwise and spanwise modulations was next performed. Each unknown field X in the frame moving with the wave $\xi = x - c\,t$, was expressed as $X(\xi, z, t) = X_0(\xi) + \varepsilon X_1(\xi, z, t)$ where $\varepsilon \ll 1$ and X_0 is the basic two-dimensional traveling wave. The perturbation X_1 was expanded as $\sum_{\varphi,k_z} \tilde{X}_{\varphi,k_z}(\xi) \exp\{i\varphi k_x \xi + i k_z z + \varsigma\, t\}$ where $\tilde{X}_{\varphi,k_z}$ is periodic in ξ with period $2\pi/k_x$, k_x being the wavenumber of the two-dimensional basic stationary wave, and k_z is the wavenumber of the transverse perturbation. Parameter φ is the detuning parameter, i.e. the ratio of the streamwise wavenumber of the perturbation to that of the basic state, hence $\varphi \in [0, 1[$. $\varphi \in \mathbb{Q}$ signals a subharmonic mode, especially $\varphi = 1/2$, and $\varphi \notin \mathbb{Q}$ an incommensurate modulated mode. Denoting $\mathbf{X_0}(\xi)$ the vector formed by the different components of the basic state, and $\tilde{\mathbf{X}}$ the vector formed by the amplitudes of the perturbations, the linearized set of equations can be formally written as

$$\varsigma \tilde{\mathbf{X}} = \mathcal{L}(\mathbf{X_0}, \partial_\xi; c, q_0, \delta, \zeta, \eta, \varphi, k_z)\, \tilde{\mathbf{X}}\,, \tag{53}$$

where $\mathcal{L}$ is a linear operator, and ς is the complex growth rate, the maximum real part of which is noted ς_r^M and corresponds to the most amplified perturbation, i.e. the one of interest from the experimental point of view. The parameter space $\varphi \times k_z$ can be reduced by invoking two symmetries: (i) the reflection of the waves in the spanwise direction, which allows us to consider only positive k_z; (ii) the real nature of the basic equations, which makes (53) invariant under the transformation $(\varphi,\, k_z,\, \varsigma,\, \tilde{\mathbf{X}}) \to (-\varphi,\, -k_z,\, \varsigma^\star,\, \tilde{\mathbf{X}}^\star)$, the star denoting complex conjugation. Thus, the parameter space $\varphi \times k_z$ can be limited to $[0,\, \frac{1}{2}] \times [0, \infty[$. For convenience, the eigenvalue problem (53) was solved in Fourier space where we used 256 real modes to represent the computed 2D waves and 128 complex modes to represent the perturbation (limited to 32 for the complete model owing to its complexity). Eigenvalues and eigenvectors were computed using a QR algorithm implemented on a RS/6000 IBM workstation.

Liu *et al.* (1995) considered a falling film of a glycerol-water mixture ($\rho = 1070\,\mathrm{kg/m^3}$, $\nu = 2.3\,10^{-6}$ m^2 s^{-1} and $\sigma = 67\,10^{-3}$ N m^{-1}), with $\beta = 6.4^\circ$ and $Re = 56$. They measured the wavelength of the 2D basic state λ_x as well as the wavelength of the transverse modulations λ_z, obtained by varying the frequency of the periodic forcing. Results of the Floquet analysis using the complete, regularized and simplified models are presented in figure 4 using dimensional units. Conversion from our dimensionless variables to dimensional scales have been made through (49). The agreement with experiments turns out to be better when streamwise and spanwise velocities are assumed to be of the same order, as done here, than by assuming that the spanwise velocity field w is of order ϵ as done in Ruyer-Quil & Manneville (2000), which is in line with the application of the least degeneracy principle. The computed wavelengths λ_x of γ_1 waves are in good agreement with experimental findings. In line with results reported by Liu *et al.* , our computations also indicate relatively small variations of λ_z with the frequency. The transverse wavelengths of the most amplified perturbations for

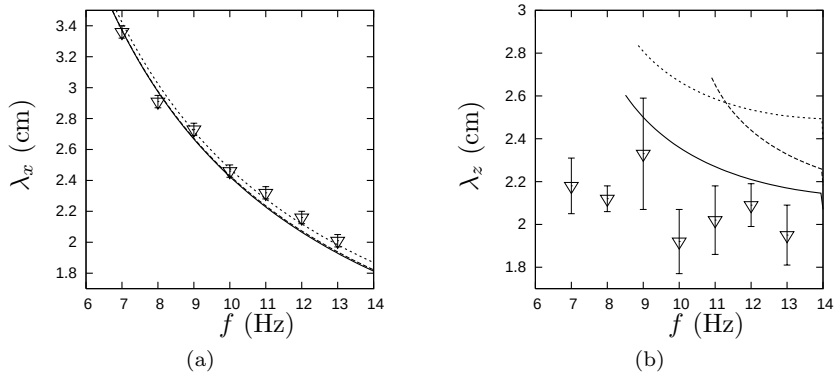

Figure 4: Streamwise wavelengths λ_x of 2D waves (a) and spanwise wavelengths λ_z (b) of the most amplified 3D perturbations versus the forcing frequency f, with $\beta = 6.4°$, $Re = 56$ and $\Gamma = 2002$. Open down triangles are experimental findings by Liu *et al.* (1995). Solid, dashed and dotted lines correspond to the complete model (63), the regularized model (52) and the simplified model, respectively. Notice that in panel (a), solid and dashed lines are superposed.

the regularized and the complete models are in good agreement, whereas the Floquet analysis of the simplified model indicates larger wavelengths. This points out the important role played by the second-order inertia terms — induced by the deviations of the velocity profile from its parabolic shape— in the mechanism of the 3D secondary instability. Yet, at low frequency, λ_z goes to infinity so that the most amplified perturbation is spanwise-uniform, while the experimental λ_z remains finite. Another difference between the results of the Floquet analysis and the experimental findings is the fact that the detuning parameter for the most amplified perturbation (not shown) systematically corresponds to a subharmonic secondary instability ($\varphi = \frac{1}{2}$) whereas Liu *et al.* reported a synchronous transition ($\varphi \approx 0$).
Figure 5(a) summarizes the experimental findings by Liu *et al.* in the $Re \times f$ plane for the same glycerol-water mixture and with $\beta = 4°$. Liu *et al.* reported two different scenarios that are strongly reminiscent of what happens in boundary layers. The first one, referred to as a *synchronous* mode, is characterized by wave crests deformed in phase in the spanwise direction. The second one, less commonly observed, appears when two successive crests are deformed with a phase shift of π. This leads to chequerboard (or herringbone) patterns characteristic of a streamwise subharmonic instability combined to a spanwise modulation. These two modes are reminiscent of aligned and staggered Λ-vortices developing in transitional boundary layers, thus analogous to the type-K and type-H transitions, respectively. Corresponding results for the stability of γ_1 waves are presented in figure 5(b-d), as obtained from the regularised model. The results for the solutions to the complete and simplified models are very similar to those obtained with the regularised model and thus not shown. We have computed the detun-

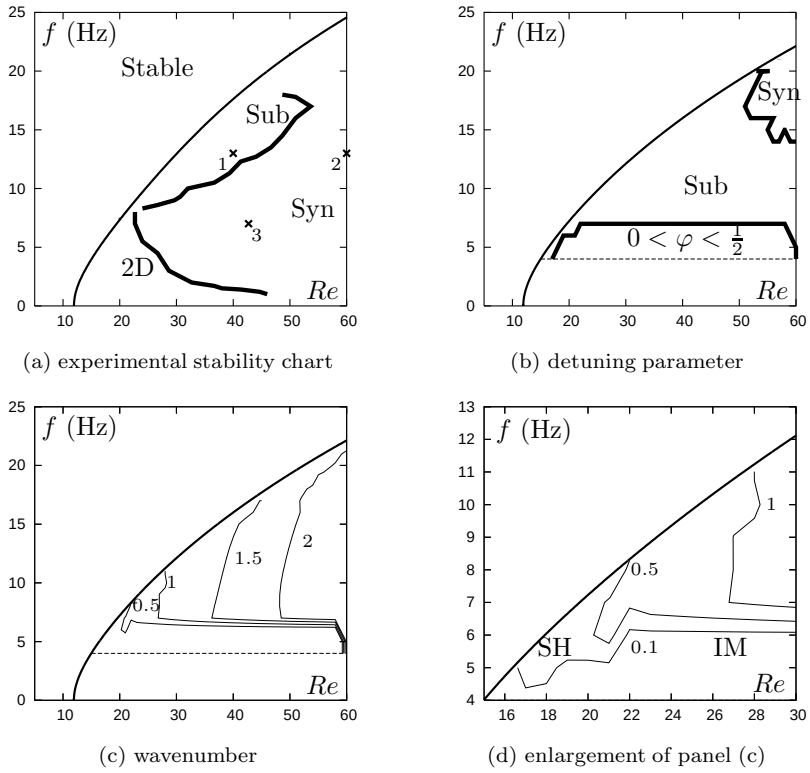

(a) experimental stability chart

(b) detuning parameter

(c) wavenumber

(d) enlargement of panel (c)

Figure 5: Stability of the γ_1 waves against 3D modes as function of the Reynolds number Re and the frequency f for $\beta = 4°$ and $\Gamma = 2340$ (Liu *et al.*, 1995, figure 6). (a) Experimental stability chart. Stability zones are bounded by thick lines : '2D' where no 3D instability was observed, 'Sub' for 3D subharmonic instability and 'Syn' for 3D synchronous instability. The neutral stability curve is represented by a thin solid line (Orr–Sommerfeld analysis). Crosses refer to parameter sets reported in table 1; (b) detuning parameter, where the synchronous (Syn) and subharmonic (Sub) instability regions correspond to $\varphi = 0$ and 0.5, respectively. (c) Wavenumber k_z of the fastest growing transverse modulation (in cm^{-1}); (d) enlargement of panel (c): 'SH' subharmonic 2D instability ($\varphi = \frac{1}{2}$), 'IM' incommensurate modulated 2D mode ($0 < \varphi < \frac{1}{2}$). Dashed lines indicate the limit (4 Hz) of the computations in panels (b, c). Results presented in panels (b-d) have been obtained using the regularised model.

Set	Re	β (deg)	Γ	f (Hz)	k	c	$\langle h \rangle$
1	40.0	4.0	2340	13	1.565	0.824	0.987
2	60.0	4.0	2340	13	1.494	0.689	0.970
3	42.7	4.0	2340	7	0.953	0.703	0.975
4	48.0	6.4	2002	10	0.980	0.628	0.965

Table 1: Dimensionless wavenumber k, phase speed c and averaged thickness $\langle h \rangle$ of the computed γ_1 waves corresponding to experimental conditions by Liu *et al.* (1995). The constant mean flow rate condition $\langle q \rangle = 1/3$ was enforced. Parameters are the Reynolds number R, the inclination β, the Kapitza number Γ and the forcing frequency f.

ing parameter (figure 5*b*) and the spanwise wavenumber (figure 5*c,d*) of the fastest growing perturbation, with a Reynolds step of 1 and a frequency step of 1 Hz (the lowest frequency considered is 4 Hz owing to the large number of modes necessary to represent the solution in that case). Computations show that k_z decreases steadily as Re is lowered and goes to zero in a region close to the neutral stability curve (see figure 5*d*). This rapid decrease of k_z corresponds to the boundary separating two and three-dimensional secondary instabilities, which agrees well with the results of Liu *et al.* who reported two-dimensional flows mainly close to the threshold of the primary instability (see figure 5*a*). In this small region, the γ_1 waves undergo a subharmonic 2D instability ($\varphi = \frac{1}{2}$). At low frequency and large Reynolds number, the instability is also found to be 2D ($k_z = 0$) but corresponds to an incommensurate mode ($\varphi \in]0, \frac{1}{2}[$). This provides an indication that the frontier between two and three-dimensional flows may exist and is not an experimental artifact due to finite-size effects. At low frequency and large Reynolds number, Floquet stability analysis of γ_1 waves predicts a 2D region wider than reported in experiments, which can be understood if one keeps in mind that γ_2 waves are likely to develop in that region of the parameter plane in place of γ_1 waves, the stability of which is considered in this section.

As already mentioned, computations predict an overwhelming presence of the subharmonic scenario ($\varphi = \frac{1}{2}$) whereas Liu *et al.* observed it only close to the neutral stability curve at large frequencies and large Reynolds numbers. In fact, computations predict a region of synchronous 3D instability at large Reynolds numbers only using the regularized model. Figure 6 shows the isocontours of the growth rate ς_r of the fastest growing perturbation in the plane $\varphi \times k_z$ for the three models, corresponding to the set #2 of table 1. The complete and the regularized models agree well with each other for the selection of the fastest growing spanwise wavenumber, whereas the simplified model predicts longer spanwise wavelengths. Moreover, figures 6(*a,b*) show that ς_r varies very little with the detuning parameter φ. Indeed, for the complete and the regularized models, the growth rates for $\varphi = 0$ and $\varphi = \frac{1}{2}$ are close to each other so that the instability does not discriminate. On the contrary, the simplified model is more selective (see figure 6*c*) and clearly predicts a subharmonic instability. This result points out again

the subtle role of the second-order inertia terms in the pattern selection. Figure 7 presents isocontours of ς_r in the $\varphi \times k_z$ plane for the parameter

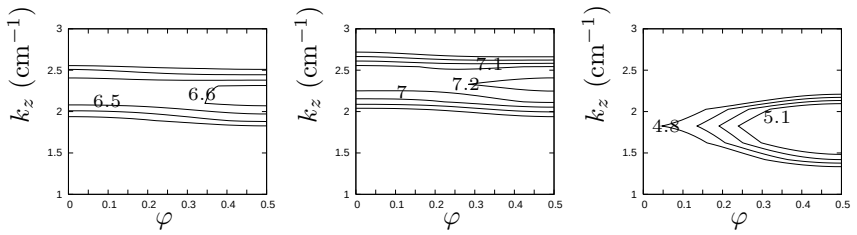

(a) complete (b) regularized (c) simplified

Figure 6: Maximum growth rate in s^{-1} as function of the detuning parameter φ and the transverse wavenumber k_z in cm^{-1}, computed with the different models for set #2.

set #3 of table 1. Results obtained with the complete model are not shown since they are close to those corresponding to the regularized model. It is clear that the detuning parameter does not significantly affect the growth rate and the instability does again not discriminate. However, comparing figure 7(a) to figure 7(b), one can see that the growth rate of the fastest growing perturbations of the γ_1 waves is again more sensitive to the detuning parameter φ with the simplified model than with the regularized one.

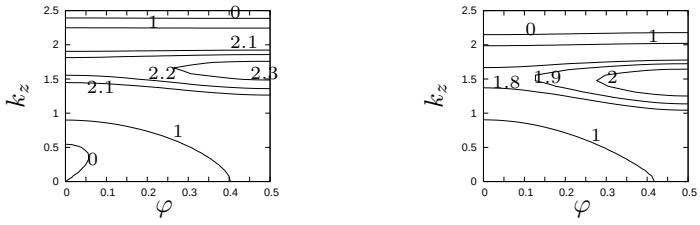

(a) regularized (b) simplified

Figure 7: Same caption as for figure 6 with parameter set #3.

The direct correspondence between results from the Floquet analysis and the experiments is based on three assumptions. First, the γ_1 waves emerge from the primary instability. Second, a broadband white noise is assumed. Third, the 2D waves are assumed to saturate before the onset of the 3D instability. As indicated by Liu *et al.*, the irregularities at the distributor are time-independent and preferentially trigger in-phase modulations of the evolving 3D patterns. Therefore experimental noise contains a larger part of in-phase perturbations than out-of-phase disturbances, which may trigger the synchronous instability easier than the subharmonic mode, given that they have growth rates close to each other. Indeed Liu *et al.* were compelled to apply controlled perturbations to enforce subharmonic instabilities. Pre-

cisely because inlet noise may contain significant spanwise perturbations, 3D instabilities may arise before the saturation of the 2D waves has a chance to develop. Such a sensitivity to inlet conditions can only be checked by direct numerical simulations of the models.

8 Two-dimensional simulations of three-dimensional flows

Floquet analysis predicts that the subharmonic scenario is predominant, which contradicts experimental observations. This discrepancy has been understood by considering that the secondary instability does not discriminate well, since the maximum growth rate is nearly identical over the whole range $0 \leq \varphi \leq 1/2$ of the detuning parameter. This property makes the 3D instability strongly dependent on the initial conditions, and thus prevents one to relate univocally the results of the Floquet analysis to the experimental findings.

In this section we therefore perform time integrations of the complete model (63), the regularized model (52) and the simplified model obtained when taking $\mathcal{G}_{\|} = 1$. Periodic boundary conditions in both x and z directions are imposed. This allows us to make use of the good convergence properties of spectral methods. A pseudo-spectral scheme has been developed, with derivatives evaluated in Fourier space and nonlinearities in physical space. The time dependence is accounted for by a fifth-order Runge-Kutta scheme, which allows controlling the error by difference with an embedded fourth-order scheme (see details in Press *et al.* (1992)). In practice, the time step is adapted to limit the relative error on each variable to 10^{-4}. The explicit character of the algorithm makes it easy to implement the different models. The computational domain of size $L_x \times L_z$ is discretised with $M \times N$ regularly spaced grid points with coordinates $x_i = iL_x/M$ and $z_j = jL_z/N$. The three-dimensionality of the waves is evaluated through:

$$E_x(t) \equiv \frac{1}{MN} \sum_{j=1}^{N} \left(\sum_{m=1}^{M/2-1} |a_m(z_j,t)|^2 \right)^{1/2}, \tag{54a}$$

$$E_z(t) \equiv \frac{1}{MN} \sum_{i=1}^{M} \left(\sum_{n=1}^{N/2-1} |b_n(x_i,t)|^2 \right)^{1/2}, \tag{54b}$$

where the spatial Fourier coefficients a_m and b_n are defined by

$$a_m(z,t) = \sum_{i=0}^{M/2-1} \left[h(x_{2i},z,t) + \mathrm{i}\, h(x_{2i+1},z,t) \right] \exp\left[2\pi \mathrm{i}\, mi/(M/2) \right], \tag{54c}$$

$$b_n(x,t) = \sum_{j=0}^{N/2-1} \left[h(x,z_{2j},t) + \mathrm{i}\, h(x,z_{2j+1},t) \right] \exp\left[2\pi \mathrm{i}\, nj/(N/2) \right], \tag{54d}$$

and where i stands for the imaginary unit. E_x and E_z are the streamwise

and the spanwise energy of deformations (Joo & Davis, 1992; Press *et al.*, 1992).
Owing to the spatial periodicity in the streamwise direction, the simulations physically correspond to a closed flow where the averaged film thickness is conserved in the domain. As mentioned there, the flow being gravity-oriented, the closed-flow condition cannot be achieved experimentally and the open flow condition should be used instead. Indeed, the conservation condition in the moving reference frame (see details in Scheid *et al.* (2005*b*)):

$$\langle h \rangle_{\xi} = \frac{\langle q \rangle_{\xi} - Q}{c} \tag{55}$$

shows that the averaged thickness $\langle h \rangle$ can be significantly lower than the inlet thickness, depending on the wave characteristics c and q_0. Therefore, in order to improve comparisons of simulations to experimental data, we can turn to our advantage the closed-flow condition inherent in the numerical scheme by imposing a film thickness tuned to the value obtained from (55) for 2D travelling waves at the corresponding forcing frequency using AUTO97. Doing so ensures that we "embark" the right amount of liquid in the computational domain lying under the 2D travelling waves. Since the local flow rate varies as the cube of the local film thickness, this trick can be crucial in recovering experimental results. Thus, the development of 2D waves undergoing 3D instabilities is simulated by enforcing initial conditions in the form:

$$h(x,z,0) = \langle h \rangle + A_x \cos(2\pi n_x x/L_x) + A_z \cos(2\pi n_z z/L_z) + A_{\text{noise}} \tilde{r}(x,z)\,, \tag{56}$$

where $A_x, A_z, A_{\text{noise}}$ are small amplitudes, $n_x, n_z \in \mathbb{N}$ represent the numbers of sinusoidal waves in each direction, and $\tilde{r}$ is a random function with values in the interval $[-1,1]$. The last term of (56) accounts for ambient white noise whose amplitude is set to $A_{\text{noise}} = 10^{-3}$. Moreover, in order to facilitate comparison with experimental results, we will keep the aspect ratio of the computational domain equal to unity by setting $L_x = L_z \equiv L$. The value of L must be taken large enough to allow complex flow dynamics. The general form of (56) enables us to explore a wide range of experimental results on 3D waves emerging from 2D waves. In the following, we consider 3D modulations of γ_1 waves, γ_2 waves and natural (i.e. noise-driven) waves. In practice we are interested in domains with lengths fitting an integer number of the travelling waves under consideration.
The presence of high nonlinearities ψ in the regularized model ($\psi = 7$ for 64b and $\psi = 5$ for 64c) can have a dramatic effect in terms of aliasing, which should thus be carefully treated. It can be proven that applying a lowpass filter such that only the first $m' = 2/(\psi+1)$ modes are kept, fully saves us from aliasing errors. This means in our case that 3/4 ($m' = 1/4$) of the modes should be shut down at each time step and thus not be used to represent the corresponding solution. Consequently, to maintain the spatial resolution as first expected, we would have to increase by 4 the number of mesh points in each direction. This is most of the time prohibitive but hopefully unnecessary. Indeed, since the higher nonlinearities only arise

from the small inertia corrections in the streamwise equation (64b), the value of $m' = 1/3$ (i.e. $\psi = 5$) appears to be always fine. In fact, even $m' = 2/3$ has been safely used for all simulations presented in the following, except $m' = 1/2$ for two cases (sets #7 and #8) when the wave structure becomes too sharp and needs higher frequencies to be properly resolved.

8.1 3D modulations of γ_1 waves

We first consider the transition from 2D γ_1 waves to 3D patterns, which corresponds to the experimental results by Liu *et al.* (1995). Their well-controlled experiments will also serve as a benchmark for a systematic evaluation of the accuracy and usefulness of the different models.
Liu *et al.* have imposed a spanwise-uniform periodic forcing. In an attempt to mimic their experiments, we set $A_x = 0.1$ and $A_z = 0$ in (56). L is set equal to five times the wave length $2\pi/k$ of the precursor 2D travelling wave, i.e. $n_x = 5$. The numbers of grid points for the simulations in this section are $M \times N = 128 \times 64$, hence 64×32 Fourier modes, or effectively 42×21 modes due to the aliasing treatment.
The values of the parameters for the different numerical experiments are indicated in table 1. We first start by considering flow conditions for an inclination angle $\beta = 4^\circ$ and Kapitza number $\Gamma = 2340$ (sets #1-3 in table 1 and in figure 5*a*). Each chosen couple (frequency,Reynolds number) is indicated by a cross in figure 5*a*. Set #1 corresponds to the region of the plane (f, Re) where herringbone patterns were observed experimentally, i.e. subharmonic instability. Simulations of the complete, regularized and simplified models agree with both the Floquet analysis and the experimental data by showing the presence of staggered crests and troughs. Isothickness contours of the wave patterns are shown at different times in figure 8 for the regularized model: At its final stage (figure 8*c*), the film evolves towards a staggered arrangement of smooth and large bumps, and thin and deep depressions that agrees well with the experimental observations.
Using the parameter set #2, we move next to the region in figure 5*a* where synchronous secondary instability has been reported by Liu *et al.* (1995) whereas the Floquet analysis predicts a subharmonic instability (compare figure 5*a* to figure 5*d*). Time integrations of the different models, given in figure 9 for the same spanwise energy of deformation E_z, show disagreement: The complete model (panel *a*) shows a sideband instability, $\varphi \ll 1$, leading to a synchronous pattern while from the simplified model (panel *c*) one gets staggered troughs and more deformed crests indicating a subharmonic instability, $\varphi = \frac{1}{2}$. Solution to the regularized model (figure 9*b*) corresponds to a combination of synchronous and staggered modulations, while seeming closer to the solution to the complete model (and experimental observations) than to the solution to the simplified one: (i) crests are hardly deformed whereas troughs tend to form deep isolated depressions; (ii) spanwise and streamwise wavelengths have values close to each other (four spanwise modulations for the complete and regularized model, in contrast with three for the simplified one); (iii) nonlinear docking of two neighboring depressions (the two downside right in figure 9*a* and the two upside left in

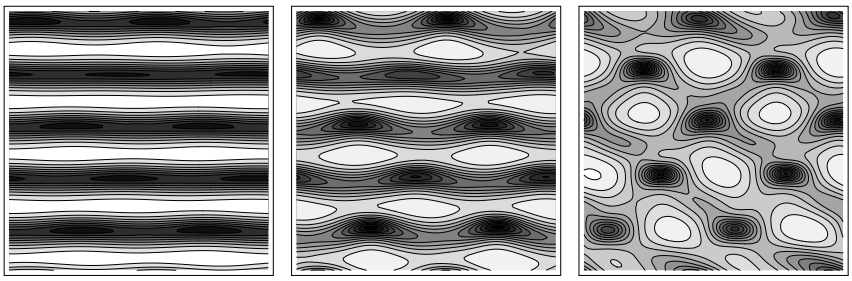

(a) t=150 (b) t=175 (c) t=195

Figure 8: Snapshots of free surface deformations giving rise to an herringbone pattern, computed for the parameter set #1 (see table 1) with the regularized model at different times. Isothickness contours are separated by an elevation step of 0.06. The numbers of grid points are $M \times N = 128 \times 64$ and $L = 2n_x\pi/k$. Amplitudes of the initial periodic forcing are $A_x = 0.1$ and $A_z = 0$, with $n_x = 5$. Dark and bright zones stand for depressions and elevations respectively.

figure 9*b*). This is in line with the fact that as seen in figure 6(*a,b*), the sec-

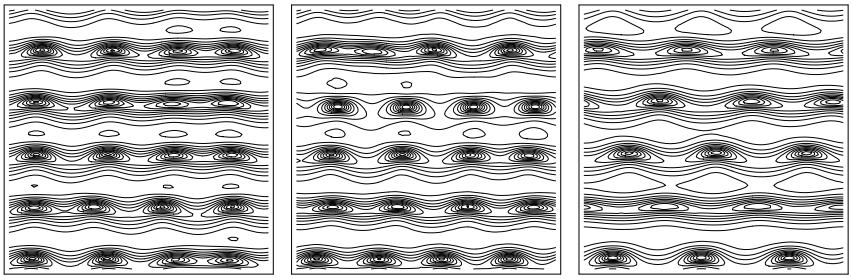

(a) complete, t=125 (b) regularized, t=125 (c) simplified, t=155

Figure 9: Snapshots of free surface deformations computed for parameter set #2 at $E_z \approx 0.05$ for the three models. Isothickness contours are separated by a level difference of 0.08. See also caption of figure 8. Note that the shading have been removed for clearness.

ondary instability does not discriminate for the parameter set #2. On the other hand, as expected from the linear prediction (figure 6*c*), the simplified model clearly selects the subharmonic instability, ending in a staggered pattern (figure 9*c*). Similar behaviors of the three models (not shown here) have been also found for parameter set #3.

Parameter set #4 of table 1 corresponds to a more pronounced inclination angle ($\beta = 6.4°$) and thus to a smaller Kapitza number ($\Gamma = 2002$). Simulations indicate that if the initial excitation is spanwise uniform ($A_z = A_{\text{noise}} = 0$), the 2D steady state corresponds to an oscillatory mode instead of a travelling wave. This is illustrated in figure 10 by plotting in (*a*) the

time evolution of the streamwise deformation energy E_x and in (b) the wave profiles at two different times corresponding to a maximum (label '1') and a minimum (label '2') of E_x during one oscillating period. Such an oscillatory mode has been numerically and called *quasi-periodic* (Ramaswamy *et al.*, 1996). The direct numerical simulations of the equations indicate that the quasi-periodic regime is widely present in the case of a vertical plane when the Reynolds number becomes large. In the vocabulary of dynamical systems theory, the flow tends to a torus (quasi-periodic regime), instead of evolving towards a limit cycle in phase space (travelling wave). This behavior is generated by the destabilization of the existing limit cycle and can be predicted by looking at the maximum growth rate of Floquet perturbations, the imaginary part of which was also found to be positive for the parameter set #4.

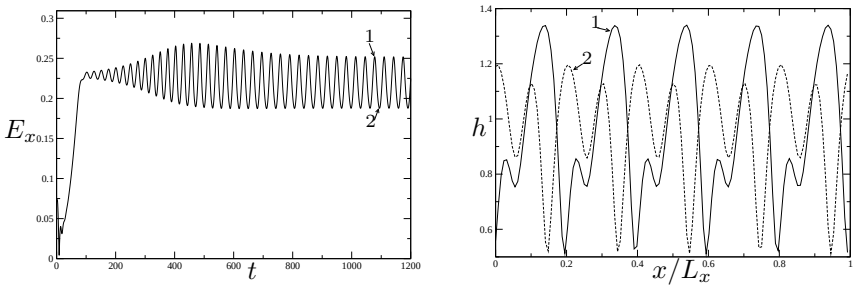

(a) (b)

Figure 10: (a) Energy of streamwise deformations E_x computed for parameter set #4 as function of time; (b) corresponding 2D wave profiles. The complete model (63) has been used for computations and $A_x = 0.1$, $A_z = 0$, $A_{\text{noise}} = 0$, $n_x = 5$, $L_x = 10\pi/k$ for the initial condition.

The wave patterns for the different models are shown in figure 11. The amplitude of the initial streamwise modulations is $A_x = 0.2$ ($A_z = A_{\text{noise}} = 0$). We see that both the complete and the simplified models yield staggered patterns whereas the regularized model yields a synchronous pattern, in agreement with experimental data (Liu *et al.*, 1995). In fact, it appears that the onset of the 3D pattern is strongly influenced by the presence of the 2D oscillatory mode and then by the exchange of energy between this mode and the 3D instability mode. This exchange depends on the initial conditions and in particular on the amplitude A_x of the initial streamwise modulations. Figure 12 shows 3D wave patterns computed with the regularized model for two different values of A_x. Significant qualitative differences can be noted by comparing them to figure 11(b): At low initial amplitude A_x, the final transverse modulations seem to have longer wavelengths than at larger values of A_x. Furthermore, crests display out-of-phase modulations whereas modulations are clearly in-phase when the initial amplitude A_x is increased. Time evolutions of the energies E_x and E_z are displayed in figure 13. When $A_x = 0.1$, the system clearly approaches the unstable stationary wave solution and remains close to it for a long time. There-

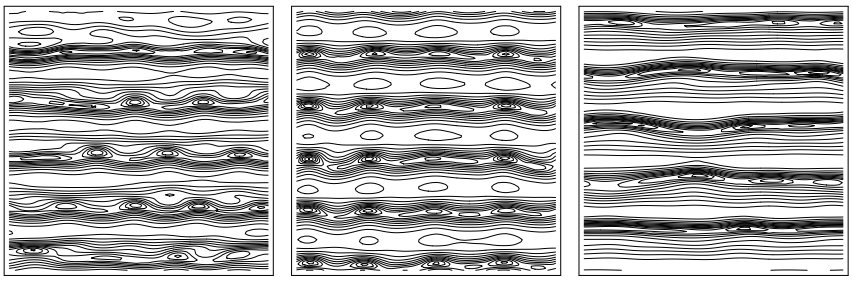

(a) complete, t=345 (b) regularized, t=305 (c) simplified, t=295

Figure 11: Free surface deformations computed for the parameter set #4 at $E_z \approx 0.05$ for the three models. Isothickness contours are separated by an elevation step of 0.06. Amplitude of the initial forcing is here $A_x = 0.2$.

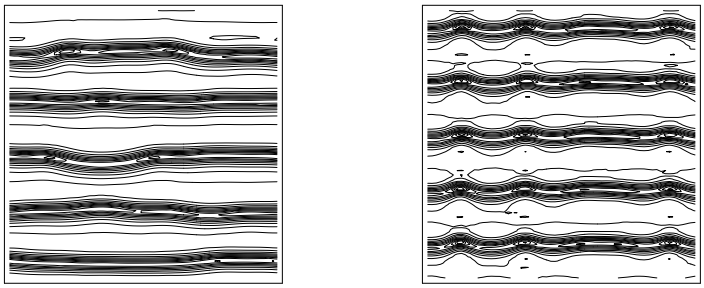

(a) regularized, A_x=0.1 (b) regularized, A_x=0.3

Figure 12: Free surface deformations computed for the parameter set #4 at $E_z \approx 0.05$: (a) $t = 300$, (b) $t = 220$.

fore, the Floquet analysis still applies and the obtained staggered pattern corresponds to the predicted subharmonic instability. This is no longer the case for larger values of A_x where the modulation of the 2D wave-train occurs prior to the development of the 3D instability. The observed synchronous pattern is thus the complex result of two ingredients: the growing 2D oscillations and the 3D instability.

We have already noticed how sensitive the pattern formation is to the initial conditions, due to the poor discrimination of the secondary instability. Nevertheless, experiments show a clear selection of the synchronous instability, most probably triggered by the small defects of the inlet distributor. In order to mimic such inlet inhomogeneities in simulations, an $x-$independent noise $\tilde{r}'(z)$ has been added to the initial condition (56), whose amplitude $A^{(z)}_{\text{noise}}$ represents the inlet roughness. A realistic estimate of about 1μm roughness gives an amplitude of $A^{(z)}_{\text{noise}} = 0.01$ for a typical film thickness of 100μm. Figures 14 and 15 display results obtained with the regularised model, as compared to those obtained experimentally (Liu *et al.*, 1995, figures 7 and 11). They show the influence of such a perturbation, which

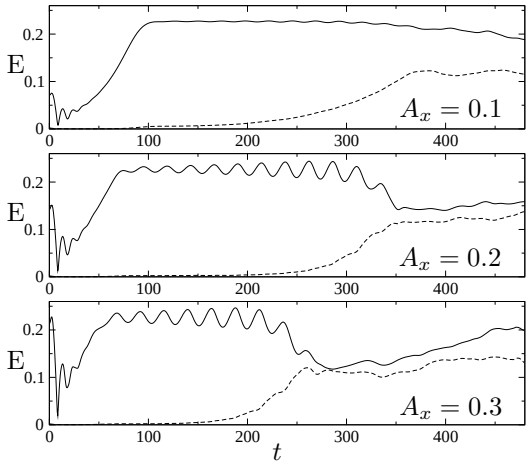

Figure 13: Deformation energies computed for parameter set #4 using the regularized model (52) and various values of A_x. Solid and dashed lines correspond to E_x and E_z, respectively. Figures 12(a), 11(b) and 12(b) correspond to pictures taken at times when E_z crosses the level 0.05.

effectively bias the evolution in favour of the synchronous instability. To facilitate comparisons with the experimental results, numerical snapshots are separated in the vertical direction by the distance covered by the waves between the two times at which the snapshots have been taken (roughly 14.2 cm and 5.8 cm in the case of figures 14 and 15 respectively). The agreement with experiments is now reasonable even though, mostly because of the choice of periodic boundary conditions, some differences can still be noticed. The spanwise wavelength selected in the simulation shown in figure 14 seems to be a little smaller than in the experiment (37 mm in comparison to roughly 46 mm), whereas in the case of figure 15, the simulation and the experiment give essentially the same answer (28 mm as compared to 26 mm). However, experiments and simulations share common qualitative features. Isothickness contours agree well with each other, and strong modulations of the troughs are observed, whereas the crests remain nearly undeformed, which leads to the formation of isolated depressions. In particular, as experimentally observed by Liu *et al.*, the numerical simulations here indicate the formation of local saddle points on the wave pattern corresponding to minima in the spanwise direction and maxima in the streamwise direction (see the right panel of figure 14 where one of such saddle points is indicated by a cross). Liu *et al.* have measured the difference of height between the minima of the thickness at a trough and the height of the nearby saddle point. They called it "trough transverse modulation amplitude", denoted $\Delta h_{\min}(x)$. From the measurement of $\Delta h_{\min}(x)$ at different locations for the experimental data corresponding to the parameter set #3, i.e. their figure 7 and the present figure 14, they computed a spatial growth rate of approximately $0.11\,\mathrm{cm}^{-1}$. Following a similar procedure, we define $\Delta h_{\min}(t)$ as the height difference between the minimum of the thickness in the entire

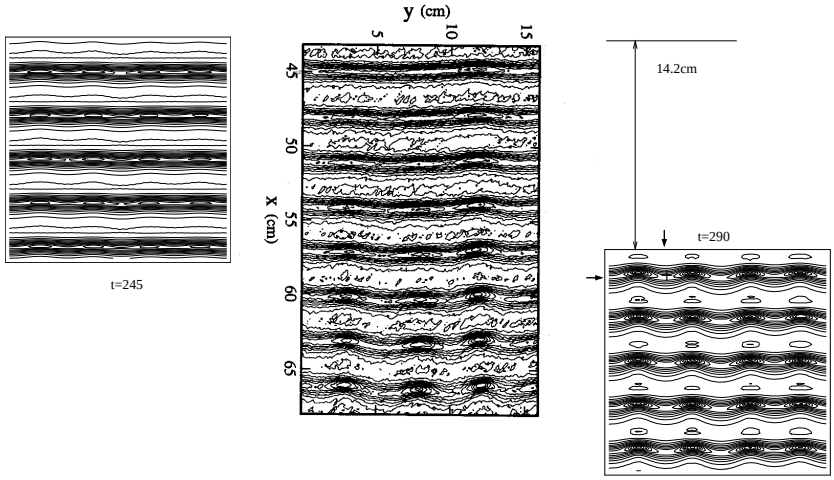

Figure 14: Snapshots of the film free surface obtained using the regularised model (52) at two different times, along with the experimental picture in the centre (Liu *et al.*, 1995, figure 7). Parameters correspond to set #3 in table 1. $A_x = 0.2$, $n_x = 5$, $A_z = 0$, $L = 2n_x\pi/k$, $A_{\text{noise}} = 10^{-3}$, an x-independent noise with amplitude $A^{(z)}_{\text{noise}} = 10^{-2}$ is added to mimic the effect of inlet roughness. The size of the computational domain is 148×148 mm. Isothickness contours are separated by an elevation step of 0.06. The location of a saddle point in the right snapshot (see text) is indicated by a cross and two arrows.

computational domain and the closest saddle point at a given time t. From the measurement of $\Delta h_{\min}(t)$ in the simulation, a temporal growth rate is found to be approximately $2.6\,\mathrm{s}^{-1}$, which is converted into a spatial growth rate, $0.125\,\mathrm{cm}^{-1}$, hence of the correct order of magnitude, with the help of the speed of the corresponding 2D γ_1 waves, $20.8\,\mathrm{cm\,s}^{-1}$.

Let us emphasize that good agreements between computer simulations and experiments exists provided that initial conditions are appropriately tuned. The widespread observation of the synchronous instability in experiments thus seems to result from the presence of spanwise non-uniformities at inlet, which favors in-phase modulations of the wave fronts. In fact, the synchronous instability of the slow γ_1 branch was not found in previous studies focused on vertically falling films where the streamwise dissipation effects were also neglected (Chang, 1994; Trifonov, 1989). This shows that the small inclination of the plane and the streamwise dissipation both play a role in the onset of the synchronous scenario.

Comparisons of computer simulations of the complete, regularized and simplified models to the experimental results by Liu *et al.* (1995) show that the streamwise second-order inertia terms, which result from the departure of the velocity profile from its parabolic flat-film shape, play a crucial role in the onset of the synchronous instability. In the case of the simplified model,

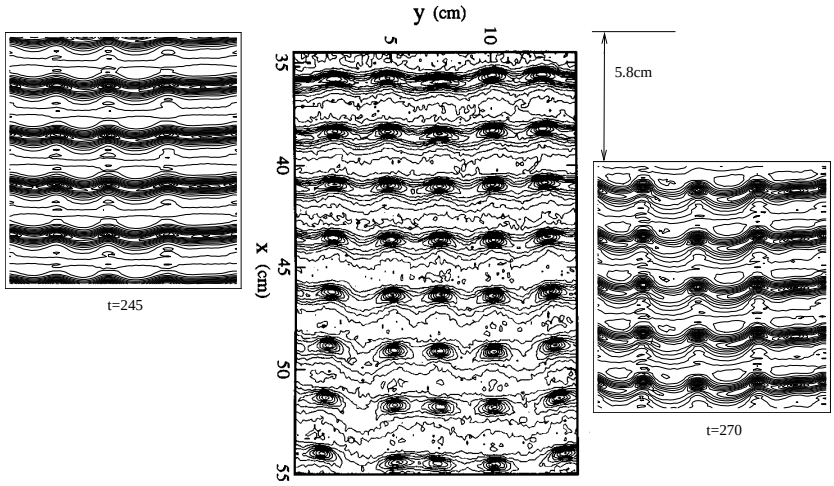

Figure 15: Same caption as for figure 14 with the parameter set #4 (Liu *et al.*, 1995, figure 11). The size of the computational domain is 118 × 118 mm. Isothickness contours are separated by an elevation step of 0.08.

which does not take the second-order inertia correction into account, the secondary instability is much more selective in favor of the subharmonic scenario. The complete model (seven equations) and the regularized model (three equations) give results in reasonably good agreement with experimental data in all cases. This agreement is likely due to the recasting of the second-order inertia corrections using the regularization technique described in Part I and applied here to yield (52). This procedure ensured that the second-order terms remain small compared to the first-order ones for the widest possible range of parameter values. For this reason, we believe that the regularized model is a useful and accurate alternative to the full-scale numerical simulations for a large range of parameter values. It contains the salient features that play a significant role in the dynamics of film flows. Therefore, the regularized model (52) will be the only model used from now to compare theory with experimental findings.

8.2 3D modulations of γ_2 waves

In this section, we consider the experimental conditions investigated by Park & Nosoko (2003) who observed 3D wave patterns emerging from 2D waves of γ_2-type on a vertical wall. Parameter values corresponding to the different numerical experiments are given in table 2. Park & Nosoko (2003) have imposed a periodic modulation in the spanwise direction, which biased the selection towards synchronous patterns. These authors placed an array of regularly spaced needles with period $\lambda_{z,\mathrm{ndl}}$ at the inlet. The initial conditions (56) corresponding to the inlet conditions imposed by Park &

Set	Re	β	Γ	f	$\lambda_{z,\mathrm{ndl}}$	k	c	$\langle h \rangle$	k_z
5	20.7	90	3375	15.0	10	0.3461	0.900	0.899	0.699
6	20.9	90	3375	19.0	30	0.4720	0.832	0.911	0.233
7	40.8	90	3375	19.1	20	0.3845	0.714	0.912	0.377
8	59.3	90	3375	17.0	20	0.3126	0.630	0.955	0.393

Table 2: Parameters of the simulations corresponding to the experiments by Park & Nosoko (2003) for a vertical plane and pure water at 25°C. $\lambda_{z,\mathrm{ndl}}$ is the spanwise intervals of the needle array and k_z is the corresponding dimensionless wavenumber. The dimensionless wavenumber k, phase speed c and average thickness $\langle h \rangle$ of the corresponding 2D γ_2 waves are also given.

Nosoko and adapted to the present simulations are taken as: $A_x = 0.2$, $A_z = 0.05$ and $A_{\mathrm{noise}} = 0$.
Figure 16 shows snapshots for parameter set #5. Initial spanwise modula-

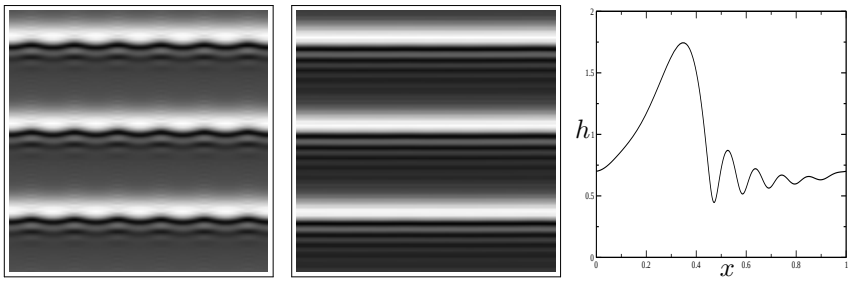

(a) $t = 27$ (b) $t = 172$ (c) $L_x = 2\pi/k$

Figure 16: (a,b) Snapshots of the film free surface at two different times computed with the regularized model and for set #5 in table 2. Initial conditions are: $A_x = 0.2$, $A_z = 0.05$, $A_{\mathrm{noise}} = 10^{-3}$, $n_x = 3$, $n_z = 6$ and $L = 2n_x\pi/k$. The computational domain is 60×60 mm with 128×128 grid points. Bright (resp. dark) zones correspond to elevations (resp. depressions). (c) 2D wave profile of (b).

tions of period $\lambda_{z,\mathrm{ndl}} = 10$ mm ($n_z = 6$) are quickly damped, i.e. $E_z \to 0$, and the pattern evolves to 2D travelling waves, i.e. $E_x \to cst$, the profile of which is given in figure 16(c). It corresponds to a γ_2 wave with a large hump preceded by capillary waves, since when the forcing frequency is small, the γ_1 slow waves are not observed and the linear inception region is immediately followed by the formation of fast γ_2 waves. Such genuine 2D waves have been observed by Park & Nosoko (2003) in the right part of their test section (figure 7(a) in that reference) while in the left part, they additionally observed large spanwise modulations with a wavelength of about $3\lambda_{z,\mathrm{ndl}}$. We recovered those modulations (not shown here) by increasing the period $\lambda_{z,\mathrm{ndl}}$ to 30 mm ($n_z = 2$). However, they also decayed (with $E_z \to 0$) but at a much smaller rate indicating that the wavelength $\lambda_z = 3$ cm is close (but still below) the cut-off wavelength for spanwise

instability.
Figure 17 shows the results for parameter set #6. In this case, the initial spanwise modulation is unstable and figures 17(*a,b*) give patterns equivalent to those observed experimentally (Park & Nosoko, 2003, figure 7*b*). To be

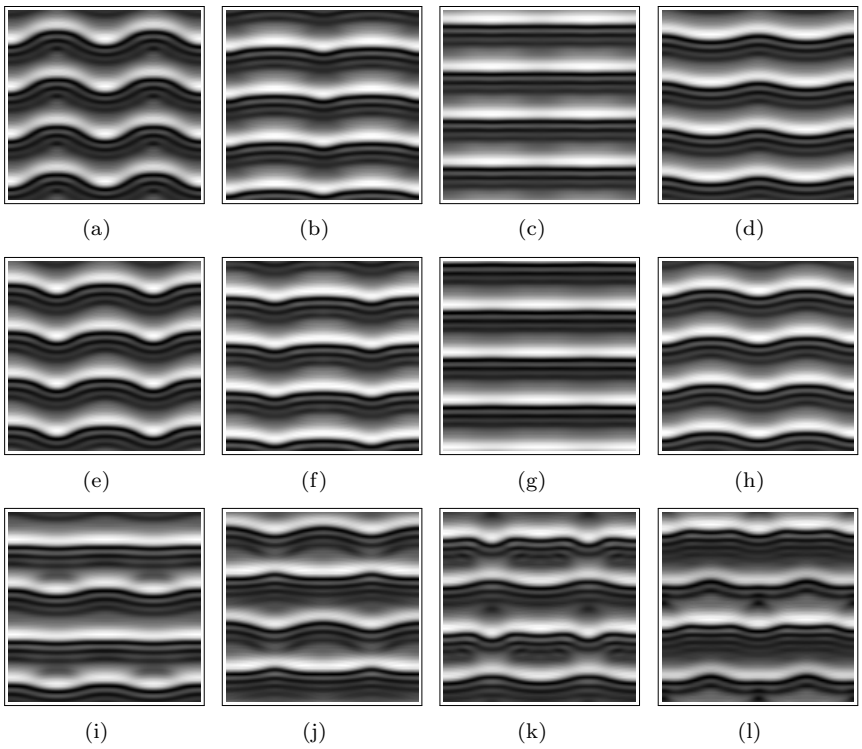

Figure 17: Simulations for the parameter set #6. See the caption of figure 16, except for $n_x = 4$, $n_z = 2$ and $L = 2n_x\pi/k$. Corresponding times are given in figure 18.

able to compare the evolution in time of computer simulations to the evolution in space of experimental waves, we need a mean to convert locations in the laboratory frame to dimensionless time in the computations. This is done by exploiting the fact that a wave travelling at speed c reaches location x at time x/c. The speeds of the 2D travelling waves corresponding to the experimental conditions have thus been computed using AUTO97. The test section in the experiments is 20 cm long which corresponds approximately to 200 dimensionless time units in the computer simulations. After running the simulation for a much longer time (1500 time units), time oscillations of the spanwise modulations were observed. Figure 18 shows that the energy of spanwise deformations E_z varies with a periodicity of about 300 time units. The region of the experimental domain corresponding to $t \approx 300$ is thus located beyond the test section, which explains why Park & Nosoko (2003) could not observe that behavior. Oscillations of shorter period (about 60 time units) can also be noticed, more pronounced for E_x

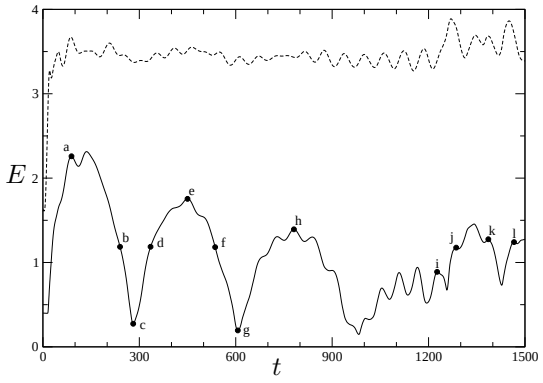

Figure 18: Deformation energies for simulations of set #6: dashed line for E_x and solid line for E_z. Letters refer to the snapshots of figure 17.

than for E_z in figure 18. Their amplitudes are small at the beginning so that it is difficult to observe their effects on the 3D wave pattern. However, they grow for $t > 900$ where they begin to influence the pattern evolution in a complex way as illustrated by the last panels (i-l) of figures 17. As time proceeds, spanwise modulations of the fronts depart more and more from their initial sinusoidal shape. The fronts start to develop rounded tips separated by flat regions. At least two symmetry breakings can be observed. The first one corresponds to a streamwise period doubling of the modulated fronts triggered by a 2D subharmonic instability, since two identical fronts are observable in panel (i) instead of four in panel (h). The second one corresponds to the development of a phase shift of π observable between the tips of two successive fronts (compare panel l to panel k).
Simulation results for a larger Reynolds number $Re = 40.8$ are presented in figure 19 (parameter set #7) and compared to experimental findings (Park & Nosoko, 2003, figure 7c). Like for $Re = 20.7$, we first observe sinusoidal spanwise modulations of the 2D waves. However, they rapidly evolve into rugged modulations, made of nearly flat backs and rounded fronts. The pattern then saturated for a while (at least during 30 time units), travelling downstream in a quasi-steady state. Notice that these rugged-modulated waves were also be observed at smaller Reynolds number (not shown) when the streamwise and spanwise initial perturbations have comparable wavelengths. In this case, they remain steady for longer time. To facilitate qualitative comparisons to the spatial evolution observed in experiments, snapshots of only a third of the numerical domain, corresponding to one streamwise wavelength, are displayed in figure 19 at increasing times. The interval of time separating each two snapshots roughly corresponds to the travelling of the fronts over a distance equal to one wavelength. Despite the use of periodic boundary conditions, the resemblance with the experimental findings (Park & Nosoko, 2003, figure 7c) is convincing. For instance the chequerboard interference pattern of the capillary waves preceding the flat zones are recovered.

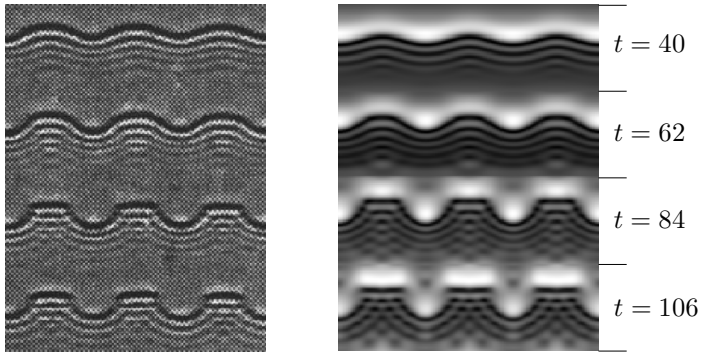

(a) (b)

Figure 19: (a) Experimental picture (real size 60×80 mm) for set #7 ($Re = 40.8$) (Park & Nosoko, 2003, figure 7*c*); (b) Simulations with $n_x = 3$, $n_z = 3$ and $L = 2n_x\pi/k$.The domain size is 60×60 mm with 256×256 grid points. Each of the four wave fronts has been obtained at a different dimensionless time, by interval of 22.

Above $Re \approx 40$, Park & Nosoko (2003) observed a breaking of the modulated fronts leading to horseshoe-like waves. Simulation results for $Re = 59.3$ are presented in figure 20 (parameter set #8) and compared to the experimental findings (Park & Nosoko, 2003, figure 7*d*). Due to computational limitations, the computational domain was limited to only one and two wavelengths in the streamwise and spanwise directions respectively ($n_x = 1$ and $n_z = 2$). As compared to $Re = 40.8$, the rugged modulations develop faster and do not saturate. Instead, the bulges of the wave front continuously expand into horseshoe-shapes, reducing the span of the flat parts at the back. As time proceeds, the legs of the horseshoes extend and split off into dimples, in qualitative agreement with experimental observations. The growth of the spanwise perturbations in the simulation is however faster than in the experiment.
In contrast with experiments by Liu *et al.* (1995) focusing on the secondary instabilities of the slow γ_1 waves, one can observe that secondary instabilities of the γ_2 waves lead neither to herringbone patterns —made of bumpy crests and deep troughs— nor to an array of isolated depressions when the instability is synchronous, but rather to modulated wave fronts.

8.3 3D natural (noise-driven) waves

In this section, we study the formation of noise-driven 3D waves in absence of periodic forcing. To match with the experiments by Alekseenko *et al.* (1994), the initial conditions (56) need to e chosen with white noise of amplitude $A_{\text{noise}} = 10^{-3}$ and $A_x = A_z = 0$. Parameter values for the different numerical experiments are given in table 3. The experimental pictures obtained by Alekseenko *et al.* (1994) are shown for reference in figure 21. Snapshots of the free surface deformation computed with the regularized

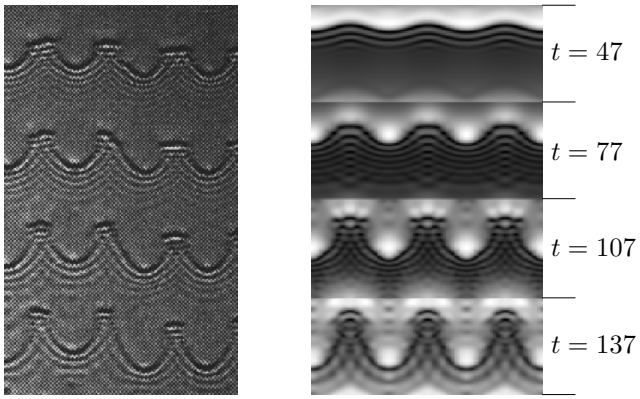

Figure 20: (a) Experimental picture (real size 60×100 mm) for set #8 ($Re = 59.3$) (Park & Nosoko, 2003, figure 7*d*); (b) Snapshots of the simulated free surface. The domain size is 40×25 mm with 256×256 grid points. Each of the four wave fronts has been obtained at increasing dimensionless times, by interval of 30.

Set	Re	β (deg)	Γ	λ_x (mm)	k	c	$\langle h \rangle$
9	8	75	1106	40	0.15	1.322	0.906
10	16	75	1106	30	0.21	1.062	0.876
11	45	75	1106	25	0.28	0.749	0.904

Table 3: Parameters of the simulations corresponding to experiments by Alekseenko *et al.* (1994) for an inclined plane and a 16% water-ethanol solution at 25°C ($\rho = 972$ kg m^{-3}, $\nu = 1.55 \times 10^{-6}$ m^2 s^{-1} and $\sigma = 40.8 \times 10^{-3}$ N m^{-1}). The 2D wave characteristics k, c and $\langle h \rangle$ have been computed from the wavelength λ_x, which has been estimated by the average streamwise separation of the 3D waves observed in the experimental pictures. See also the caption of table 1.

model are reported in figure 22 where the three columns correspond to different Reynolds numbers (sets #9-11 of table 3). Each row in figure 22 corresponds to a particular transient regime: the first row to mostly 2D waves, the second row to coalescence processes, and the two last rows to the evolution of 3D solitary waves. Since these regimes are time-dependent in simulations but space-dependent in experiments, both the dimensionless time t and the approximate location of the numerical domain on the experimental plane are given in figure 22; the distance being again estimated from the phase speed c of the 2D waves (see table 3).
Close to the inlet (first row in figure 22), the waves are mostly two-dimensional. For $Re = 8$ (panel *a*), their profile is quasi-sinusoidal —bright and dark zones occupy equivalent areas— and for $Re = 16$ (panel *b*), they become of γ_2-type with steep humps of large amplitude. For $Re = 45$ (*c*), the waves have larger crests and thinner and deeper troughs. These waves are of slow

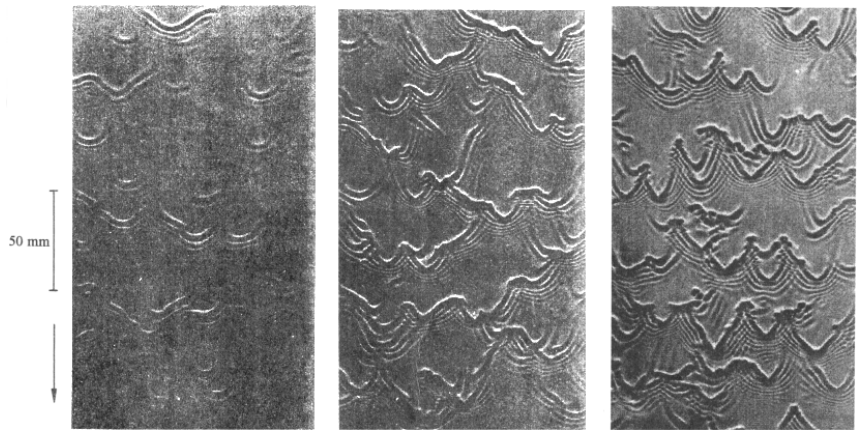

(a) $Re = 8$ (b) $Re = 16$ (c) $Re = 45$

Figure 21: Wave patterns obtained experimentally by Alekseenko *et al.* (1994) (see table 3).

γ_1-type. Dislocations (i.e. connections between two wave fronts) in the patterns are observed for the three sets.
Further downstream (second row of figure 22), three-dimensional secondary instabilities show up. The large amplitude waves travel faster and catch up the preceding slower ones, leaving an increasing flat zone behind them. As time is proceeds (third row of figure 22), fast γ_2 waves are clearly observable. The coalescence process yields solitary waves with preceding capillary ripples and large flat zones in between. Snapshots (*g,j*) and (*h,k*) of figure 22 share many similar features with experimental findings (For comparison, one should keep in mind that the grey levels represent surface elevation in simulations but surface slope in experiments). The unsteady experimental pattern is characterized by interacting quasi-steady 3D solitary waves separated by portions of constant thickness of length 10 to 50 cm.
For $Re = 8$, the average distance between the solitary waves tends to saturate for $t > 890$, which indicates that solitary waves have reached their fully developed regime. Alekseenko *et al.* (1994) did not observed such a saturation in their experiment, either because the length of their test section (not given in their book) was not long enough to observe this saturation, or because this behaviour is a consequence of the streamwise periodic boundary condition imposed in the simulations. The fact that coarsening of natural waves apparently terminates suggests that a fully developed 3D wavy regime is observable. This seems to contradict the observation by Chang *et al.* (1996*b*) that the coarsening process never ends, and that the average pulse separation increases linearly with the distance to the inlet. However, Chang *et al.* simulated a 2D vertical film using the Kapitza–Shkadov two-equation model. Several explanations can be found. First, there can be a finite-size effect in the earlier described computer simulations or the discrepancy can be attributed to limitations of their model (2D, neglect of viscous dispersion, of inclination, of nonlinear second-order inertia terms).

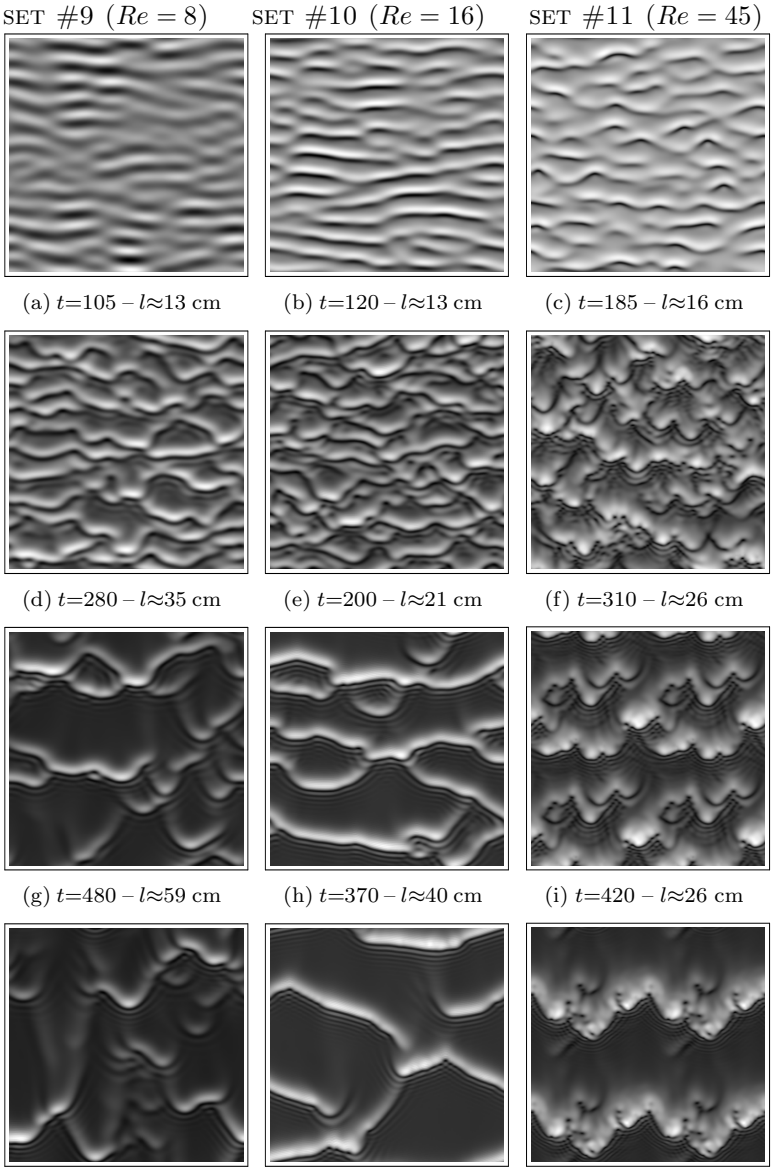

(a) t=105 – l≈13 cm (b) t=120 – l≈13 cm (c) t=185 – l≈16 cm

(d) t=280 – l≈35 cm (e) t=200 – l≈21 cm (f) t=310 – l≈26 cm

(g) t=480 – l≈59 cm (h) t=370 – l≈40 cm (i) t=420 – l≈26 cm

(j) t=890 – l≈110cm (k) t=845 – l≈91 cm (l) t=575 – l≈32 cm

Figure 22: Computer simulations of natural (noise-driven) 3D wave patterns corresponding to the experiments by Alekseenko *et al.* (1994) (see table 3). The computational domain is 100×100 mm^2 with 256×256 grid points for set #9 and #10 and 512×256 for set #11 except for panel (i) where it corresponds to 50×50 mm^2 and 256×256 grid points: the obtained snapshot is repeated four times. l is the estimated distance from the inlet. The bright (dark) zones correspond to elevations (depressions).

For $Re = 16$, saturation is not observed at all, at least during the 1500 time units of the computer simulation. In that case, the final stage corresponds to interacting oblique fronts rather than 3D horseshoe-like waves. For $Re = 45$, the 3D waves tend to form localized structures rather than extended wave fronts as it was the case for lower values of Re. This is in agreement with results of Alekseenko *et al.* (1994) and Park & Nosoko (2003) who observed V-shape or horseshoe-like solitary waves with a sharp curved front and long backwards tails under similar conditions. Yet, the transition from modulated waves to horseshoe-like solitary waves is far from understood. The region of the parameter space were the oblique solitary waves are present must be delimated.

9 Conclusions

In Part I, a short review has been presented of the modeling of film flows available in literature, insisting on the assumptions involved in their derivation and on their limits. Finite-time singularities affecting one-hump solitary-wave solutions to both one-equation (§ 3.3) and two-equation (§ 5.1) models at large δ was shown to be related to the structure of their inertia terms. Ooshida (1999)'s regularization led to equation (27) that remedies only partially to this failure since it underestimates the amplitudes and speeds of solitary waves in the drag-inertia regime.
Focusing on the treatment of inertia terms, our algebraic regularization procedure enabled us to obtain model (52a,47) which does not suffer from these limitations, and is now fully consistent with the Benney expansion up to second-order. Model (52a,47) has a complexity level that is intermediate between our previous full second-order model (52a,32) and the simplified one (52a,33). The approach developed here remedies the lack of systematism of the derivations presented in Ruyer-Quil *et al.* (2005) and Scheid *et al.* (2005*a*) where a rather *ad-hoc* argument was invoked to treat the case of a film uniformly heated from below.

In Part II, we have extended the weighted integral boundary layer models to include the spanwise dependence in order to study the transition from 2D to 3D flows. A systematic Floquet analysis of the stability of the 2D slow γ_1 waves has been performed, followed by numerical simulations using periodic boundary conditions. The aim was the description of the 3D wave patterns observed experimentally with three main objectives: (i) use experimental results as benchmarks for discriminating the different models that we have at one's disposal, namely the complete, the simplified and the regularized models; (ii) reproduce the synchronous and subharmonic transitions from γ_1 waves to 3D patterns found by Liu *et al.* (1995); (iii) recover the wave dynamics observed by Park & Nosoko (2003) in the case of well-controlled spanwise perturbations of fast γ_2 waves, and by Alekseenko *et al.* (1994) in the case of noise-driven instabilities.
Floquet analysis shows that the secondary 3D instability is not selective, since the maximum growth rate remains nearly unchanged over the whole range $0 \leq \varphi \leq 1/2$ of the detuning parameter. This property makes the 3D

instability strongly dependent on the initial conditions, and thus prevents one to relate univocally the results of Floquet analysis to experimental findings. By contrast, numerical simulations have shown good agreement with experimental results by Liu *et al.* (1995), provided that initial conditions are appropriately tuned. The widespread observation of the synchronous instability in experiments could then be attributed to the presence of spanwise non-uniformities at inlet, favouring in-phase modulations of the wave fronts. In some cases, the three-dimensional patterns emerge from a two-dimensional oscillatory mode rather than from saturated travelling waves, as also observed in direct numerical simulations by Ramaswamy *et al.* (1996). The competition between the growing 2D modulation and the secondary 3D instability makes the evolution of the film more sensitive to initial conditions. Complex 3D dynamics deep in the nonlinear regime, in particular isolated synchronous depressions (figure 15), rugged-modulated waves (figure 19) as well as horseshoe-like 3D solitary waves (figures 20 and 22*i, l*) and oblique solitary waves (figure 22*k*) found in simulations were observed in experiments.

The application of a systematic strategy to the problem of film flows is shown here to lead to systems of equations of reduced dimensionality that capture the physical mechanisms quite faithfully, helping us to enlighten the observed dynamics by isolating the important physical effects. Having reliable low-dimensional models at one's disposal allows to attack many questions still open for plain film flows over inclined planes, but also in more difficult cases, for example when heat or mass transfer are involved.

These lecture notes are the result of a collaborative work with Christian Ruyer-Quil and Paul Manneville. I would like to thank them very much for that as well as Serafim Kalliadasis and Manuel Velarde for fruitful discussions.

A Complete 2D second-order model

$$\partial_t h = -\partial_x q \tag{57}$$

$$\begin{aligned}\delta\partial_t q = {} & \frac{27}{28}h - \frac{81}{28}\frac{q}{h^2} - 33\frac{s_1}{h^2} - \frac{3069}{28}\frac{s_2}{h^2} - \frac{27}{28}\zeta h\,\partial_x h + \frac{27}{28}h\partial_{xxx}h \\ & +\delta\left[-\frac{12}{5}\frac{q s_1\partial_x h}{h^2} - \frac{126}{65}\frac{q s_2\partial_x h}{h^2} + \frac{12}{5}\frac{s_1\partial_x q}{h} + \frac{171}{65}\frac{s_2\partial_x q}{h}\right. \\ & \left.+\frac{12}{5}\frac{q\partial_x s_1}{h} + \frac{1017}{455}\frac{q\partial_x s_2}{h} + \frac{6}{5}\frac{q^2\partial_x h}{h^2} - \frac{12}{5}\frac{q\partial_x q}{h}\right] \\ & +\eta\left[\frac{5025}{896}\frac{q\left(\partial_x h\right)^2}{h^2} - \frac{5055}{896}\frac{\partial_x q\partial_x h}{h} - \frac{10851}{1792}\frac{q\partial_{xx}h}{h} + \frac{2027}{448}\partial_{xx}q\right]\end{aligned} \tag{58}$$

$$\delta\partial_t s_1 = \frac{1}{10}h - \frac{3}{10}\frac{q}{h^2} - \frac{126}{5}\frac{s_1}{h^2} - \frac{126}{5}\frac{s_2}{h^2} - \frac{1}{10}\zeta h\partial_x h + \frac{1}{10}h\partial_{xxx}h$$

$$
\begin{aligned}
&+\delta\left[-\frac{3}{35}\frac{q^2\partial_x h}{h^2}+\frac{1}{35}\frac{q\partial_x q}{h}+\frac{108}{55}\frac{qs_1\partial_x h}{h^2}-\frac{5022}{5005}\frac{qs_2\partial_x h}{h^2}\right.\\
&\left.-\frac{103}{55}\frac{s_1\partial_x q}{h}+\frac{9657}{5005}\frac{s_2\partial_x q}{h}-\frac{39}{55}\frac{q\partial_x s_1}{h}+\frac{10557}{10010}\frac{q\partial_x s_2}{h}\right] \qquad (59)\\
&+\eta\left[\frac{93}{40}\frac{q\left(\partial_x h\right)^2}{h^2}-\frac{69}{40}\frac{\partial_x h\partial_x q}{h}+\frac{21}{80}\frac{q\partial_{xx}h}{h}-\frac{9}{40}\partial_{xx}q\right]\\
\delta\partial_t s_2 \;=\;& \frac{13}{420}h-\frac{13}{140}\frac{q}{h^2}-\frac{39}{5}\frac{s_1}{h^2}-\frac{11817}{140}\frac{s_2}{h^2}-\frac{13}{420}\zeta h\partial_x h+\frac{13}{420}h\partial_{xxx}h\\
&+\delta\left[-\frac{4}{11}\frac{qs_1\partial_x h}{h^2}+\frac{18}{11}\frac{qs_2\partial_x h}{h^2}-\frac{2}{33}\frac{s_1\partial_x q}{h}\right.\\
&\left.-\frac{19}{11}\frac{s_2\partial_x q}{h}+\frac{6}{55}\frac{q\partial_x s_1}{h}-\frac{288}{385}\frac{q\partial_x s_2}{h}\right] \qquad (60)\\
&+\eta\left[-\frac{3211}{4480}\frac{q\left(\partial_x h\right)^2}{h^2}+\frac{2613}{4480}\frac{\partial_x h\partial_x q}{h}-\frac{2847}{8960}\frac{q\partial_{xx}h}{h}+\frac{559}{2240}\partial_{xx}q\right]
\end{aligned}
$$

B Complete 3D second-order model

The integral method used here consists in projecting the velocity fields as

$$
\begin{aligned}
u &= \frac{3}{h}\left(q-s_1-s_2\right)g_0(\bar{y})+45\frac{s_1}{h}g_1(\bar{y})+210\frac{s_2}{h}g_2(\bar{y})\,, \qquad (61a)\\
w &= \frac{3}{h}\left(p-r_1-r_2\right)g_0(\bar{y})+45\frac{r_1}{h}g_1(\bar{y})+210\frac{r_2}{h}g_2(\bar{y})\,, \qquad (61b)
\end{aligned}
$$

where $\bar{y}=y/h$ and the streamwise and spanwise flow rates $q=\int_0^h u\,\mathrm{d}y$ and $p=\int_0^h w\,\mathrm{d}y$, respectively, appear with two corrections each, namely s_1, s_2 and r_1, r_2, associated to the following orthogonal test functions:

$$
\begin{aligned}
g_0 &= \bar{y}-\frac{1}{2}\bar{y}^2\,, \qquad (62a)\\
g_1 &= \bar{y}-\frac{17}{6}\bar{y}^2+\frac{7}{3}\bar{y}^3-\frac{7}{12}\bar{y}^4\,, \qquad (62b)\\
g_2 &= \bar{y}-\frac{13}{2}\bar{y}^2+\frac{57}{4}\bar{y}^3-\frac{111}{8}\bar{y}^4+\frac{99}{16}\bar{y}^5-\frac{33}{32}\bar{y}^6\,. \qquad (62c)
\end{aligned}
$$

Applying the Galerkin method which consists in integrating the boundary layer equations (48), substituting the projections (61), taking the test functions (62) as weight functions, and using the boundary conditions (48*d,e,f*), yield the complete model:

$$
\begin{aligned}
\partial_t h &= -\partial_x q-\partial_z p\,, \qquad (63a)\\
\delta\,\partial_t q &= \frac{27}{28}h-\frac{81}{28}\frac{q}{h^2}-33\frac{s_1}{h^2}-\frac{3069}{28}\frac{s_2}{h^2}+\delta\left[-\frac{12}{5}\frac{qs_1\partial_x h}{h^2}-\frac{126}{65}\frac{qs_2\partial_x h}{h^2}\right.\\
&\quad+\frac{12}{5}\frac{s_1\partial_x q}{h}+\frac{171}{65}\frac{s_2\partial_x q}{h}+\frac{12}{5}\frac{q\partial_x s_1}{h}+\frac{1017}{455}\frac{q\partial_x s_2}{h}+\frac{6}{5}\frac{q^2\partial_x h}{h^2}\\
&\quad\left.-\frac{12}{5}\frac{q\partial_x q}{h}-\frac{6}{5}\frac{q\partial_z p}{h}-\frac{6}{5}\frac{p\partial_z q}{h}+\frac{6}{5}\frac{qp\partial_z h}{h^2}-\frac{6}{5}\frac{qr_1\partial_z h}{h^2}\right.
\end{aligned}
$$

$$
\begin{aligned}
&-\frac{63}{65}\frac{qr_2\partial_z h}{h^2}-\frac{6}{5}\frac{ps_1\partial_z h}{h^2}-\frac{63}{65}\frac{ps_2\partial_z h}{h^2}+\frac{6}{5}\frac{s_1\partial_z p}{h}+\frac{108}{65}\frac{s_2\partial_z p}{h}\\
&+\frac{6}{5}\frac{r_1\partial_z q}{h}+\frac{63}{65}\frac{r_2\partial_z q}{h}+\frac{6}{5}\frac{q\partial_z r_1}{h}+\frac{576}{455}\frac{q\partial_z r_2}{h}+\frac{6}{5}\frac{p\partial_z s_1}{h}+\frac{63}{65}\frac{p\partial_z s_2}{h}\Bigg]\\
&+\eta\left[\frac{5025}{896}\frac{q\left(\partial_x h\right)^2}{h^2}-\frac{5055}{896}\frac{\partial_x q\partial_x h}{h}-\frac{10851}{1792}\frac{q\partial_{xx}h}{h}+\frac{2027}{448}\partial_{xx}q+\partial_{zz}q\right.\\
&-\frac{2463}{1792}\frac{\partial_z q\partial_z h}{h}+\frac{2433}{1792}\frac{q\left(\partial_z h\right)^2}{h^2}-\frac{5361}{3584}\frac{q\partial_{zz}h}{h}+\frac{7617}{1792}\frac{p\partial_x h\partial_z h}{h^2}\\
&\left.-\frac{4749}{3584}\frac{\partial_z p\partial_x h}{h}-\frac{10545}{3584}\frac{\partial_x p\partial_z h}{h}-\frac{16341}{3584}\frac{p\partial_{xz}h}{h}+\frac{1579}{448}\partial_{xz}p\right]\\
&-\frac{27}{28}\zeta h\,\partial_x h+\frac{27}{28}h\left(\partial_{xxx}+\partial_{xzz}\right)h\,,
\end{aligned}
\tag{63b}
$$

$$
\begin{aligned}
\delta\,\partial_t s_1 \;=\;& \frac{1}{10}h-\frac{3}{10}\frac{q}{h^2}-\frac{126}{5}\frac{s_1}{h^2}-\frac{126}{5}\frac{s_2}{h^2}+\delta\left[\frac{1}{35}\frac{q\partial_x q}{h}-\frac{3}{35}\frac{q^2\partial_x h}{h^2}+\frac{108}{55}\frac{qs_1\partial_x h}{h^2}\right.\\
&-\frac{5022}{5005}\frac{qs_2\partial_x h}{h^2}-\frac{103}{55}\frac{s_1\partial_x q}{h}+\frac{9657}{5005}\frac{s_2\partial_x q}{h}-\frac{39}{55}\frac{q\partial_x s_1}{h}+\frac{10557}{10010}\frac{q\partial_x s_2}{h}\\
&-\frac{2}{35}\frac{q\partial_z p}{h}+\frac{3}{35}\frac{p\partial_z q}{h}-\frac{3}{35}\frac{qp\partial_z h}{h^2}+\frac{54}{55}\frac{qr_1\partial_z h}{h^2}+\frac{54}{55}\frac{ps_1\partial_z h}{h^2}\\
&-\frac{54}{55}\frac{r_1\partial_z q}{h}-\frac{54}{55}\frac{p\partial_z s_1}{h}-\frac{2511}{5005}\frac{ps_2\partial_z h}{h^2}-\frac{2511}{5005}\frac{qr_2\partial_z h}{h^2}+\frac{2511}{5005}\frac{r_2\partial_z q}{h}\\
&\left.+\frac{2511}{5005}\frac{p\partial_z s_2}{h}-\frac{49}{55}\frac{s_1\partial_z p}{h}+\frac{7146}{5005}\frac{s_2\partial_z p}{h}+\frac{3}{11}\frac{q\partial_z r_1}{h}+\frac{1107}{2002}\frac{q\partial_z r_2}{h}\right]\\
&+\eta\left[\frac{93}{40}\frac{q\left(\partial_x h\right)^2}{h^2}-\frac{69}{40}\frac{\partial_x h\partial_x q}{h}+\frac{21}{80}\frac{q\partial_{xx}h}{h}-\frac{9}{40}\partial_{xx}q-\frac{57}{80}\frac{\partial_z q\partial_z h}{h}\right.\\
&+\frac{81}{80}\frac{q\left(\partial_z h\right)^2}{h^2}-\frac{3}{40}\frac{q\partial_{zz}h}{h}+\frac{27}{80}\frac{p\partial_{xz}h}{h}+\frac{21}{16}\frac{p\partial_x h\partial_z h}{h^2}-\frac{63}{80}\frac{\partial_z p\partial_x h}{h}\\
&\left.-\frac{9}{40}\frac{\partial_z h\partial_x p}{h}-\frac{9}{40}\partial_{xz}p\right]-\frac{1}{10}\zeta h\partial_x h+\frac{1}{10}h\left(\partial_{xxx}+\partial_{xzz}\right)h\,,
\end{aligned}
\tag{63c}
$$

$$
\begin{aligned}
\delta\,\partial_t s_2 \;=\;& \frac{13}{420}h-\frac{13}{140}\frac{q}{h^2}-\frac{39}{5}\frac{s_1}{h^2}-\frac{11817}{140}\frac{s_2}{h^2}+\delta\left[-\frac{4}{11}\frac{qs_1\partial_x h}{h^2}+\frac{18}{11}\frac{qs_2\partial_x h}{h^2}\right.\\
&-\frac{2}{33}\frac{s_1\partial_x q}{h}-\frac{19}{11}\frac{s_2\partial_x q}{h}+\frac{6}{55}\frac{q\partial_x s_1}{h}-\frac{288}{385}\frac{q\partial_x s_2}{h}-\frac{2}{11}\frac{qr_1\partial_z h}{h^2}-\frac{2}{11}\frac{ps_1\partial_z h}{h^2}\\
&+\frac{2}{11}\frac{r_1\partial_z q}{h}+\frac{2}{11}\frac{p\partial_z s_1}{h}+\frac{9}{11}\frac{qr_2\partial_z h}{h^2}+\frac{9}{11}\frac{ps_2\partial_z h}{h^2}-\frac{9}{11}\frac{r_2\partial_z q}{h}-\frac{9}{11}\frac{p\partial_z s_2}{h}\\
&\left.-\frac{8}{33}\frac{s_1\partial_z p}{h}-\frac{10}{11}\frac{s_2\partial_z p}{h}-\frac{4}{55}\frac{q\partial_z r_1}{h}+\frac{27}{385}\frac{q\partial_z r_2}{h}-\frac{3211}{4480}\frac{q\left(\partial_x h\right)^2}{h^2}\right]\\
&+\eta\left[\frac{2613}{4480}\frac{\partial_x h\partial_x q}{h}-\frac{2847}{8960}\frac{q\partial_{xx}h}{h}+\frac{559}{2240}\partial_{xx}q+\frac{3029}{8960}\frac{\partial_z q\partial_z h}{h}-\frac{3627}{8960}\frac{q\left(\partial_z h\right)^2}{h^2}\right.\\
&\left.+\frac{299}{17920}\frac{q\partial_{zz}h}{h}-\frac{559}{1792}\frac{p\partial_x h\partial_z h}{h^2}+\frac{4927}{17920}\frac{\partial_z p\partial_x h}{h}-\frac{533}{17920}\frac{\partial_x p\partial_z h}{h}\right.
\end{aligned}
$$

$$-\frac{5993}{17920}\frac{p\partial_{xz}h}{h}+\frac{559}{2240}\partial_{xz}p\Big]-\frac{13}{420}\zeta h\partial_x h+\frac{13}{420}h\left(\partial_{xxx}+\partial_{xzz}\right)h\,, \tag{63d}$$

$$\begin{aligned}
\delta\,\partial_t p \;=\;& -\frac{81}{28}\frac{p}{h^2}-33\frac{r_1}{h^2}-\frac{3069}{28}\frac{r_2}{h^2}+\delta\left[\frac{6}{5}\frac{qp\partial_x h}{h^2}-\frac{6}{5}\frac{p\partial_x q}{h}-\frac{6}{5}\frac{q\partial_x p}{h}\right.\\
&+\frac{6}{5}\frac{p^2\partial_z h}{h^2}+\frac{6}{5}\frac{s_1\partial_x p}{h}+\frac{6}{5}\frac{r_1\partial_x q}{h}+\frac{6}{5}\frac{q\partial_x r_1}{h}+\frac{6}{5}\frac{p\partial_x s_1}{h}-\frac{6}{5}\frac{qr_1\partial_x h}{h^2}\\
&-\frac{6}{5}\frac{ps_1\partial_x h}{h^2}-\frac{63}{65}\frac{qr_2\partial_x h}{h^2}-\frac{63}{65}\frac{ps_2\partial_x h}{h^2}+\frac{63}{65}\frac{s_2\partial_x p}{h}+\frac{63}{65}\frac{q\partial_x r_2}{h}\\
&+\frac{108}{65}\frac{r_2\partial_x q}{h}-\frac{12}{5}\frac{pr_1\partial_z h}{h^2}-\frac{12}{5}\frac{p\partial_z p}{h}+\frac{12}{5}\frac{r_1\partial_z p}{h}+\frac{12}{5}\frac{p\partial_z r_1}{h}\\
&\left.+\frac{171}{65}\frac{r_2\partial_z p}{h}+\frac{576}{455}\frac{p\partial_x s_2}{h}-\frac{126}{65}\frac{pr_2\partial_z h}{h^2}+\frac{1017}{455}\frac{p\partial_z r_2}{h}\right]\\
&+\eta\left[\frac{5025}{896}\frac{p(\partial_z h)^2}{h^2}-\frac{5055}{896}\frac{\partial_z p\partial_z h}{h}-\frac{10851}{1792}\frac{p\partial_{zz}h}{h}-\frac{2463}{1792}\frac{\partial_x p\partial_x h}{h}\right.\\
&-\frac{5361}{3584}\frac{p\partial_{xx}h}{h}+\partial_{xx}p+\frac{1579}{448}\partial_{xz}q+\frac{2027}{448}\partial_{zz}p+\frac{2433}{1792}\frac{p(\partial_x h)^2}{h^2}\\
&\left.+\frac{7617}{1792}\frac{q\partial_x h\partial_z h}{h^2}-\frac{10545}{3584}\frac{\partial_z q\partial_x h}{h}-\frac{4749}{3584}\frac{\partial_x q\partial_z h}{h}-\frac{16341}{3584}\frac{q\partial_{xz}h}{h}\right]\\
&-\frac{27}{28}\zeta h\,\partial_z h+\frac{27}{28}h\left(\partial_{xxz}+\partial_{zzz}\right)h\,,
\end{aligned} \tag{63e}$$

$$\begin{aligned}
\delta\,\partial_t r_1 \;=\;& -\frac{3}{10}\frac{p}{h^2}-\frac{126}{5}\frac{r_1}{h^2}-\frac{126}{5}\frac{r_2}{h^2}+\delta\left[-\frac{3}{35}\frac{p^2\partial_z h}{h^2}-\frac{3}{35}\frac{qp\partial_x h}{h^2}+\frac{3}{35}\frac{q\partial_x p}{h}\right.\\
&+\frac{1}{35}\frac{p\partial_z p}{h}-\frac{2}{35}\frac{p\partial_x q}{h}+\frac{54}{55}\frac{qr_1\partial_x h}{h^2}+\frac{54}{55}\frac{ps_1\partial_x h}{h^2}-\frac{54}{55}\frac{s_1\partial_x p}{h}\\
&-\frac{54}{55}\frac{q\partial_x r_1}{h}+\frac{3}{11}\frac{p\partial_x s_1}{h}-\frac{49}{55}\frac{r_1\partial_x q}{h}+\frac{108}{55}\frac{pr_1\partial_z h}{h^2}-\frac{103}{55}\frac{r_1\partial_z p}{h}\\
&-\frac{39}{55}\frac{p\partial_z r_1}{h}+\frac{1107}{2002}\frac{p\partial_x s_2}{h}-\frac{5022}{5005}\frac{pr_2\partial_z h}{h^2}-\frac{2511}{5005}\frac{qr_2\partial_x h}{h^2}-\frac{2511}{5005}\frac{ps_2\partial_x h}{h^2}\\
&\left.+\frac{2511}{5005}\frac{s_2\partial_x p}{h}+\frac{2511}{5005}\frac{q\partial_x r_2}{h}+\frac{9657}{5005}\frac{r_2\partial_z p}{h}+\frac{7146}{5005}\frac{r_2\partial_x q}{h}+\frac{10557}{10010}\frac{p\partial_z r_2}{h}\right]\\
&+\eta\left[-\frac{69}{40}\frac{\partial_z p\partial_z h}{h}+\frac{93}{40}\frac{p(\partial_z h)^2}{h^2}+\frac{21}{16}\frac{q\partial_x h\partial_z h}{h^2}-\frac{3}{40}\frac{p\partial_{xx}h}{h}+\frac{81}{80}\frac{p(\partial_x h)^2}{h^2}\right.\\
&+\frac{27}{80}\frac{q\partial_{xz}h}{h}+\frac{21}{80}\frac{p\partial_{zz}h}{h}-\frac{57}{80}\frac{\partial_x p\partial_x h}{h}-\frac{63}{80}\frac{\partial_x q\partial_z h}{h}-\frac{9}{40}\partial_z q\partial_x h-\frac{9}{40}\partial_{xz}q\\
&\left.-\frac{9}{40}\partial_{zz}p\right]-\frac{1}{10}\zeta h\partial_z h+\frac{1}{10}h(\partial_{xxz}h+\partial_{zzz}h)\,,
\end{aligned} \tag{63f}$$

$$\begin{aligned}
\delta\,\partial_t r_2 \;=\;& -\frac{13}{140}\frac{p}{h^2}-\frac{39}{5}\frac{r_1}{h^2}-\frac{11817}{140}\frac{r_2}{h^2}+\delta\left[-\frac{2}{35}\frac{p\partial_x q}{h}-\frac{2}{11}\frac{qr_1\partial_x h}{h^2}-\frac{2}{11}\frac{ps_1\partial_x h}{h^2}\right.\\
&+\frac{2}{11}\frac{s_1\partial_x p}{h}+\frac{2}{11}\frac{q\partial_x r_1}{h}-\frac{4}{55}\frac{p\partial_x s_1}{h}-\frac{8}{33}\frac{r_1\partial_x q}{h}-\frac{4}{11}\frac{pr_1\partial_z h}{h^2}-\frac{2}{33}\frac{r_1\partial_z p}{h}\\
&\left.+\frac{6}{55}\frac{p\partial_z r_1}{h}+\frac{27}{385}\frac{p\partial_x s_2}{h}+\frac{18}{11}\frac{pr_2\partial_z h}{h^2}+\frac{9}{11}\frac{qr_2\partial_x h}{h^2}+\frac{9}{11}\frac{ps_2\partial_x h}{h^2}\right.
\end{aligned}$$

$$
\begin{aligned}
&-\frac{9}{11}\frac{s_2\partial_x p}{h}-\frac{9}{11}\frac{q\partial_x r_2}{h}-\frac{19}{11}\frac{r_2\partial_z p}{h}-\frac{10}{11}\frac{r_2\partial_x q}{h}-\frac{288}{385}\frac{p\partial_z r_2}{h}\Bigg]\\
&+\eta\left[+\frac{2613}{4480}\frac{\partial_z p\partial_z h}{h}-\frac{3211}{4480}\frac{p(\partial_z h)^2}{h^2}-\frac{559}{1792}\frac{q\partial_x h\partial_z h}{h^2}+\frac{299}{17920}\frac{p\partial_{xx}h}{h}\right.\\
&-\frac{3627}{8960}\frac{p(\partial_x h)^2}{h^2}-\frac{5993}{17920}\frac{q\partial_{xz}h}{h}-\frac{2847}{8960}\frac{p\partial_{zz}h}{h}+\frac{3029}{8960}\frac{\partial_x p\partial_x h}{h}\\
&\left.+\frac{4927}{17920}\frac{\partial_x q\partial_z h}{h}-\frac{533}{17920}\partial_z q\partial_x h+\frac{559}{2240}\partial_{xz}q+\frac{559}{2240}\partial_{zz}p\right]\\
&-\frac{13}{420}\zeta h\partial_z h+\frac{13}{420}h(\partial_{xxz}h+\partial_{zzz}h)\,, \qquad (63g)
\end{aligned}
$$

C Regularized second-order model

$$
\begin{aligned}
\partial_t h &= -\partial_x q-\partial_z p\,. \qquad (64a)\\
\delta\,\partial_t q &= \delta\left[\frac{9}{7}\frac{q^2}{h^2}\partial_x h-\frac{17}{7}\frac{q}{h}\partial_x q\right]+\left\{\frac{5}{6}h-\frac{5}{2}\frac{q}{h^2}+\delta\left[-\frac{8}{7}\frac{q\partial_z p}{h}-\frac{9}{7}\frac{p\partial_z q}{h}\right.\right.\\
&\quad\left.+\frac{9}{7}\frac{qp\partial_z h}{h^2}\right]+\eta\left[4\frac{q\left(\partial_x h\right)^2}{h^2}-\frac{9}{2}\frac{\partial_x q\partial_x h}{h}-6\frac{q\partial_{xx}h}{h}+\frac{9}{2}\partial_{xx}q\right.\\
&\quad+\frac{13}{4}\frac{p\partial_x h\partial_z h}{h^2}-\frac{\partial_z q\partial_z h}{h}-\frac{43}{16}\frac{\partial_x p\partial_z h}{h}-\frac{13}{16}\frac{\partial_z p\partial_x h}{h}+\frac{3}{4}\frac{q\left(\partial_z h\right)^2}{h^2}\\
&\quad\left.-\frac{23}{16}\frac{q\partial_{zz}h}{h}-\frac{73}{16}\frac{p\partial_{xz}h}{h}+\partial_{zz}q+\frac{7}{2}\partial_{xz}p\right]\\
&\quad\left.-\frac{5}{6}\zeta h\,\partial_x h+\frac{5}{6}h\left(\partial_{xxx}+\partial_{xzz}\right)h\right\}\left(1-\frac{\delta}{70}q\partial_x h\right)^{-1}, \qquad (64b)\\
\delta\,\partial_t p &= \delta\left[\frac{9}{7}\frac{p^2}{h^2}\partial_z h-\frac{17}{7}\frac{p}{h}\partial_z p\right]-\frac{5}{2}\frac{p}{h^2}+\delta\left[-\frac{8}{7}\frac{p\partial_x q}{h}-\frac{9}{7}\frac{q\partial_x p}{h}+\frac{9}{7}\frac{qp\partial_x h}{h^2}\right]\\
&\quad+\eta\left[4\frac{p\left(\partial_z h\right)^2}{h^2}-\frac{9}{2}\frac{\partial_z p\partial_z h}{h}-6\frac{p\partial_{zz}h}{h}+\frac{9}{2}\partial_{zz}p+\frac{13}{4}\frac{q\partial_x h\partial_z h}{h^2}\right.\\
&\quad-\frac{\partial_x p\partial_x h}{h}-\frac{43}{16}\frac{\partial_z q\partial_x h}{h}-\frac{13}{16}\frac{\partial_x q\partial_z h}{h}+\frac{3}{4}\frac{p\left(\partial_x h\right)^2}{h^2}-\frac{23}{16}\frac{p\partial_{xx}h}{h}\\
&\quad\left.-\frac{73}{16}\frac{q\partial_{xz}h}{h}+\partial_{xx}p+\frac{7}{2}\partial_{xz}q\right]-\frac{5}{6}\zeta h\,\partial_z h+\frac{5}{6}h\left(\partial_{xxz}+\partial_{zzz}\right)h\,, \qquad (64c)
\end{aligned}
$$

References

Alekseenko, S., Nakoryakov, V. & Pokusaev, B. 1994 *Wave flow in liquid films*, 3rd edn. Begell House (New York).

Argyriadi, K., Serifi, K. & Bontozoglou, V. 2004 Nonlinear dynamics of inclined films under low-frequency forcing. *Phys. Fluids* **16** (7), 2457–2468.

Benney, D. 1966 Long waves on liquid films. *J. Math. Phys.* **45**, 150–155.

Brevdo, L., Laure, P., Dias, F. & Bridges, T. 1999 Linear pulse structure and signaling in a film flow on an inclined plane. *J. Fluid Mech.* **396**, 37–71.

Chang, H.-C. 1994 Wave evolution on a falling film. *Ann. Rev. Fluid Mech.* **26**, 103–136.

Chang, H.-C., Cheng, M., Demekhin, E. & Kopelevitch, D. 1994 Secondary and tertiary excitation of three-dimensional patterns on a falling films. *J. Fluid Mech.* **270**, 251–275.

Chang, H.-C., Demekhin, E. & Kalaidin, E. 1996*a* Simulation of noise-driven wave dynamics on a falling film. *AIChE J.* **42**, 1553–1568.

Chang, H.-C., Demekhin, E., Kalaidin, E. & Ye, Y. 1996*b* Coarsening dynamics of falling-film solitary waves. *Phys. Rev. E* **54**, 1467–1477.

Chang, H.-C., Demekhin, E. & Kopelevitch, D. 1993 Nonlinear evolution of waves on a vertically falling film. *J. Fluid Mech.* **250**, 433–480.

Doedel, E., Champneys, A., Fairfrieve, T., Kuznetsov, Y., Sandstede, B. & Wang, X. 1997 Auto 97 continuation and bifurcation software for ordinary differential equations. *Montreal Concordia Univ.* .

Floryan, J., Davis, S. & Kelly, R. 1987 Instabilities of a liquid film flowing down a slightly inclined plane. *Phys. Fluids* **30**, 983–989.

Gjevik, B. 1970 Occurrence of finite-amplitude surface waves on falling liquid films. *Phys. Fluids* **13**, 1918–1925.

Gjevik, B. 1971 Spatially varying finite-amplitude wave trains on falling liquid films. *Acta Polytech. Scand. Me.* **61**, 1–16.

Glendinning, P. & Sparrow, C. 1984 Local and global behavior near homoclinic orbits. *J. Stat. Phys.* **35**, 645–696.

Herbert, T. 1988 Secondary instability of boundary layers. *Ann. Rev. Fluid Mech.* **20**, 487.

Joo, S. & Davis, S. 1992 Instabilities of three-dimensional theory viscous falling films. *J. Fluid Mech.* **242**, 529.

Kapitza, P. 1948 Wave flow of thin layers of a viscous fluid: I. free flow - II. fluid flow in the presence of continuous gas flow and heat transfer. In *Collected papers of P.L. Kapitza* (ed. D. T. Haar), pp. 662–689. Pergamon 1965, (Original paper in Russian: Zh. Ekper. Teor. Fiz. **18**, I. 3–18, II. 19–28).

Kapitza, P. & Kapitza, S. 1949 Wave flow of thin layers of a viscous fluid: III. experimental study of undulatory flow conditions. In *Collected papers of P.L. Kapitza* (ed. D. T. Haar), pp. 690–709. Pergamon 1965, (Original paper in Russian: Zh. Ekper. Teor. Fiz. **19**, 105–120).

Lin, S. 1974 Finite amplitude side-band stability of a viscous fluid. *J. Fluid Mech.* **63**, 417–429.

Liu, J. & Gollub, J. 1993 Onset of spatially chaotic waves on flowing films. *Phys. Rev. Lett.* **70**, 2289–2292.

Liu, J. & Gollub, J. 1994 Solitary wave dynamics of film flows. *Phys. Fluids* **6**, 1702–1712.

Liu, J., Paul, J. & Gollub, J. 1993 Measurements of the primary instabilities of film flows. *J. Fluid Mech.* **250**, 69–101.

Liu, J., Schneider, J. & Gollub, J. 1995 Three-dimensional instabilities of film flows. *Phys. Fluids* **7**, 55–67.

Nakaya, C. 1975 Long waves on a viscous fluid down a vertical wall. *Phys. FluidsA* **18**, 1407–1412.

Nosoko, T. & Miyara, A. 2004 The evolution and subsequent dynamics of waves on a vertically falling liquid film. *Phys. Fluids* **16** (4), 1118–1126.

Nosoko, T., Yoshimura, P., Nagata, T. & Okawa, K. 1996 Characteristics of two-dimensional waves on a falling liquid film. *Chem. Eng. Sci.* **51**, 725–732.

Ooshida, T. 1999 Surface equation of falling film flows with moderate reynolds number and large but finite weber number. *Phys. Fluids* **11**, 3247–3269.

Panga, M. & Balakotaiah, V. 2003 Low-dimensional models for vertically falling viscous films. *Phys. Rev. Lett.* **90** (15), 1.

Park, C. D. & Nosoko, T. 2003 Three-dimensional wave dynamics on a falling film and associated mass transfer. *AIChE J.* **49** (11), 2715–2727.

Press, W., Teukolsky, S., Vetterling, W. & Flannery, B. 1992 *Numerical recipes in C - The Art of Scientific Computing*, 2nd edn. Cambridge University Press(New York).

Pumir, A., Manneville, P. & Pomeau, Y. 1983 On solitary waves running down an inclined plane. *J. Fluid Mech.* **135**, 27–50.

Ramaswamy, B., Chippada, S. & Joo, S. 1996 A full-scale numerical study of interfacial instabilities in thin-film flows. *J. Fluid Mech.* **325**, 163–194.

Roberts, A. 1996 Low-dimensional models of thin film fluid dynamics. *Phys. Lett. A* **212**, 63–71.

Ruyer-Quil, C. & Manneville, P. 1998 Modeling film flows down inclined planes. *Eur. Phys. J. B* **6**, 277–292.

Ruyer-Quil, C. & Manneville, P. 2000 Improved modeling of flows down inclined planes. *Eur. Phys. J. B* **15**, 357–369.

Ruyer-Quil, C. & Manneville, P. 2002 Further accuracy and convergence results on the modeling of flows down inclined planes by weighted-residual approximations. *Phys. Fluids* **14**, 170–183.

Ruyer-Quil, C. & Manneville, P. 2004 Comment on "low-dimensional models for vertically falling viscous films". *Phys. Rev. Lett.* **93**, 199401.

Ruyer-Quil, C., Scheid, B., Kalliadasis, S., Velarde, M. & Zeytounian, R. 2005 Thermocapillary long waves in a liquid film flow. part 1. low dimensional formulation. *J. Fluid Mech.* **538**, 199–222.

Salamon, T., Armstrong, R. & Brown, R. 1994 Traveling waves on vertical films: Numerical analysis using the finite element method. *Phys. Fluids* **5**, 2202.

Scheid, B., Ruyer-Quil, C., Kalliadasis, S., Velarde, M. G. & R. Kh. Zeytounian 2005*a* Thermocapillary long waves in a liquid film flow. part 2. linear stability and nonlinear waves. *J. Fluid Mech.* **538**, 223–244.

Scheid, B., Ruyer-Quil, C., Thiele, U., Kabov, O., Legros, J.-C. & Colinet, P. 2005*b* Validity domain of the Benney equation including the Marangoni effect for closed and open flows. *J. Fluid Mech.* **527**, 303–335.

Schlichting, H. 1979 *Boundary-Layer Theory*, seventh edn. Mc Graw-Hill.

Schmid, P. J. & Henningson, D. S. 2001 *Stability and transition in shear flows*. Springer, Berlin.

Shkadov, V. 1967 Wave flow regimes of a thin layer of viscous fluid subject to gravity. *Izv. Ak. Nauk SSSR, Mekh. Zhidk Gaza, Mekh. Zhi. Gaza* **1**, 43–51, english translation in *Fluid Dynamics***2** (Faraday Press, N.Y., 1970), 29-34.

Shkadov, V. 1977 Solitary waves in a layer of viscous liquid. *Izv. Ak. Nauk SSSR, Mekh. Zhidk Gaza, Mekh. Zhi. Gaza* **1**, 63–66.

Smith, M. 1990 The mechanism for the long-wave instability in thin liquid films. *J. Fluid Mech.* **217**, 469–485.

Trifonov, Y. Y. 1989 Bifurcations of two-dimensional into three-dimensional wave regimes for a vertically flowing liquid film. *Izv. Ak. Nauk SSSR, Mekh. Zhidk Gaza, Mekh. Zhi. Gaza* **5**, 109–114.

Vlachogiannis, M. & Bontozoglou, V. 2001 Observations of solitary wave dynamics of film flows. *J. Fluid Mech.* **435**, 191.

Whitham, G. 1974 *Linear and Nonlinear Waves*. John Wiley & Sons.

Yih, C.-S. 1955 Stability of two-dimensional parallel flows for three dimensional disturbances. *Quart. Appl. Math.* **12**, 434.